

# A Stellar Dynamical Measurement of the Black Hole Mass in the Maser Galaxy NGC 4258

Christos Siopis<sup>1,2</sup>, Karl Gebhardt<sup>3</sup>, Tod R. Lauer<sup>4</sup>, John Kormendy<sup>3</sup>, Jason Pinkney<sup>5</sup>,  
Douglas Richstone<sup>1</sup>, S. M. Faber<sup>6</sup>, Scott Tremaine<sup>7</sup>, M. C. Aller<sup>1</sup>, Ralf Bender<sup>8</sup>, Gary  
Bower<sup>9</sup>, Alan Dressler<sup>10</sup>, Alexei V. Filippenko<sup>11</sup>, Richard Green<sup>12</sup>, Luis C. Ho<sup>10</sup>, and John  
Magorrian<sup>13</sup>

## ABSTRACT

We determine the mass of the black hole at the center of the spiral galaxy NGC 4258 by constructing axisymmetric dynamical models of the galaxy. These models are constrained by high spatial resolution imaging and long-slit spectroscopy of the nuclear region obtained with the *Hubble Space Telescope*, complemented

---

<sup>1</sup>Department of Astronomy, University of Michigan, Ann Arbor, MI 48109-1042; siopis@umich.edu, maller@umich.edu, dor@umich.edu

<sup>2</sup>Institut d'Astronomie et d'Astrophysique, Université Libre de Bruxelles, CP 226, Boulevard du Triomphe, 1050 Bruxelles, Belgium; christos.siopis@ulb.ac.be

<sup>3</sup>Department of Astronomy, University of Texas, RLM 15.308, Austin, TX 78712; gebhardt@astro.as.utexas.edu, kormendy@astro.as.utexas.edu

<sup>4</sup>National Optical Astronomy Observatories, P. O. Box 26732, Tucson, AZ 85726; lauer@noao.edu

<sup>5</sup>Department of Physics and Astronomy, Ohio Northern University, 525 S Main St, Ada, OH 45810; j-pinkney@onu.edu

<sup>6</sup>UCO/Lick Observatory, University of California, Santa Cruz, CA 95064; faber@ucolick.org

<sup>7</sup>School of Natural Sciences, Institute for Advanced Study, Einstein Drive, Princeton, NJ 08540; tremaine@ias.edu

<sup>8</sup>Universitäts-Sternwarte, Scheinerstraße 1, München 81679, Germany; bender@usm.uni-muenchen.de

<sup>9</sup>Computer Sciences Corporation, Space Telescope Science Institute, 3700 San Martin Drive, Baltimore, MD 21218; bower@stsci.edu

<sup>10</sup>The Observatories of the Carnegie Institution of Washington, 813 Santa Barbara St., Pasadena, CA 91101; dressler@ociw.edu, lho@ociw.edu

<sup>11</sup>Department of Astronomy, University of California, Berkeley, CA 94720-3411; alex@astro.berkeley.edu

<sup>12</sup>Large Binocular Telescope Observatory, 933 N. Cherry, Tucson, AZ 85721-0065; rgreen@as.arizona.edu

<sup>13</sup>Rudolf Peierls Centre for Theoretical Physics, University of Oxford, Keble Road, Oxford, OX1 3RH, UK; j.magorrian1@physics.ox.ac.uk

by ground-based observations extending to larger radii. Our best mass estimate is  $M_{\bullet} = (3.3 \pm 0.2) \times 10^7 M_{\odot}$  for a distance of 7.28 Mpc (statistical errors only). This is within 15% of  $(3.82 \pm 0.01) \times 10^7 M_{\odot}$ , the mass determined from the kinematics of water masers (rescaled to the same distance) assuming they are in Keplerian rotation in a warped disk. The construction of accurate dynamical models of NGC 4258 is somewhat compromised by an unresolved active nucleus and color gradients, the latter caused by variations in the stellar population and/or obscuring dust. Depending on how these effects are treated, as well as on assumptions about the ellipticity and inclination of the galaxy, we obtain black hole masses ranging from  $2.4 \times 10^7 M_{\odot}$  to  $3.6 \times 10^7 M_{\odot}$ . This spread is mainly due to uncertainties in the stellar mass profile inside the central  $2''$  ( $\sim 70$  pc). Obscuration of high-velocity stars by circumnuclear dust (possibly associated with the masing disk) could lead to an underestimate of the black hole mass which is hard to correct. These problems are not present in the  $\sim 30$  other black hole mass determinations from stellar dynamics that have been published by us and other groups; thus, the relatively close agreement between the stellar dynamical mass and the maser mass in NGC 4258 enhances our confidence in the black hole masses determined in other galaxies from stellar dynamics using similar methods and data of comparable quality.

*Subject headings:* galaxies: spiral — galaxies: individual (NGC 4258) — galaxies: kinematics and dynamics — galaxies: nuclei

## 1. INTRODUCTION

The characterization of massive dark objects (hereafter “black holes”) at the centers of nearby galaxies has advanced considerably in the past decade. Nonetheless the dynamical modeling of both stellar and gas kinematics remains subject to uncertainties. These can arise from, among other things, systematic uncertainties and noise amplification in the de-projection of the observables from two to three dimensions, the presence of dust that can affect both the mass-to-light ratio ( $M/L$ ) and the observed kinematics, variations in  $M/L$  due to stellar population gradients, and the presence of nonstellar point and/or continuum sources in the central galactic regions which may swamp the light from the surrounding stars or gas. Gas kinematics can also be affected by nongravitational forces, random velocities and pressure support, which are difficult to model accurately, while the complex phase-space structure of stellar orbits can make it difficult to properly sample initial conditions and the phase-space density distribution of the orbits in (stellar) galactic equilibria. Reverberation

mapping presents a third possibility for determining black hole masses but comes with its own set of limitations (e.g., Blandford & McKee 1982; Peterson 1993; Netzer & Peterson 1997; Gebhardt et al. 2000b).

It is therefore desirable to test the reliability of these methods. Unfortunately, comparing stellar dynamical estimates to gas dynamical estimates of black hole masses is not usually possible, as few galaxies have properties that permit more than one method to be applied with confidence. Even in those cases where it is possible, a detailed comparison is not always illuminating due to uncertainties in the measurements. One case where gas dynamical and stellar dynamical mass measurements are available for the same galaxy is not reassuring: the gas dynamical mass for the black hole in IC 1459 is a factor of  $\sim 5$  smaller than the stellar dynamical mass (Verdoes Kleijn et al. 2000; Cappellari et al. 2002). Better agreement, within a factor of  $\sim 2$ , was found between the mass estimate of the black hole in Centaurus A by Silge et al. (2005) from stellar dynamics, and by Marconi et al. (2006) from gas dynamics. Even in the case of the supermassive black hole in the nucleus of our own Milky Way Galaxy, the mass estimates from individual stellar orbits (Ghez et al. 2005) and from a statistical analysis of radial velocities and proper motions (Chakrabarty & Saha 2001) differ by about a factor of two.

NGC 4258 presents a unique opportunity to test the reliability of black hole mass estimators. Miyoshi et al. (1995) and Herrnstein et al. (1999) used the Very Long Baseline Array (VLBA) to observe water maser emission in a thin, warped, and nearly edge-on gas annulus located at 0.16–0.28 pc from the center of this galaxy, and determined that a central black hole with a mass  $M_{\bullet} = (3.9 \pm 0.1) \times 10^7 M_{\odot}$  is needed to account for the observed velocity profile, proper motions, and accelerations. This black hole mass is thought to be quite reliable for several reasons. (i) The maser emission lines are both strong and narrow, lending themselves to VLBA observations of much higher resolution than possible with the *Hubble Space Telescope* (*HST*) or ground-based telescopes. (ii) The masers seem to lie in a disk that is very thin (height/radius  $\approx 0.02$ ), so the corrections to the rotation curve due to pressure or random velocities are negligible. (iii) Most importantly, the maser velocities scale very nearly as  $v(r) \propto r^{-1/2}$  with distance  $r$  from the center, so that they exhibit an almost perfect Keplerian motion, which makes the deduction of the black hole mass easy and almost free of assumptions. (iv) Finally, the measurements of the mass and distance from the radial velocities, proper motions, and accelerations of the masers are all consistent. More recently, Herrnstein et al. (2005), using a maximum likelihood analysis of the maser positions and velocities, quantified the deviation from Keplerian motion. A number of different models that can explain this discrepancy yield central masses in the range  $(3.59\text{--}3.88) \times 10^7 M_{\odot}$  rescaled to a distance of 7.28 Mpc. The warped disk model, which the authors consider the most probable, implies  $M_{\bullet} = (3.82 \pm 0.01) \times 10^7 M_{\odot}$  at this distance.

In this paper, we estimate the mass of the central black hole of NGC 4258 via modeling of the stellar dynamics of the galaxy. This is accomplished using the orbit superposition tools developed by our collaboration (the “Nuker” team) (Gebhardt et al. 2000a; Bower et al. 2001; Gebhardt et al. 2003; Thomas et al. 2004). Alternative orbit superposition tools have been developed by van der Marel et al. (1998), Cretton et al. (1999), and Valluri et al. (2004). Because the maser black hole mass estimate seemed very accurate, we intended this to be a thorough, end-to-end test of the accuracy of our method, at least for this galaxy. Unfortunately, we encountered a number of problems that hindered our ability to determine unambiguously the mass density profile in the central region of the galaxy. In particular, (i) it was not possible to accurately subtract the light of the unresolved active galactic nucleus (AGN) at the center of the galaxy to recover the underlying stellar luminosity profile; (ii) it was not possible to reliably determine the stellar  $M/L$  profile within  $\sim 2''$  of the nucleus due to a color gradient, presumably caused by diffuse dust and/or a spatial variation in the stellar population; and (iii) it was not possible to estimate the extinction caused by a compact dust patch near the nucleus, which may be obscuring light from fast-moving stars very close to the black hole, thus causing a systematic underestimate of the black hole mass.

Despite these difficulties, our “most trusted” estimate,  $M_{\bullet} = (3.3 \pm 0.2) \times 10^7 M_{\odot}$ , is in reasonable agreement with the maser mass estimate. The quoted error margin corresponds to the “ $1\sigma$ ” confidence band, and reflects statistical errors only. Uncertainties in the mass profile discussed in the previous paragraph widen the error margin to  $2.4 \times 10^7 M_{\odot} < M_{\bullet} < 3.6 \times 10^7 M_{\odot}$ . This range still does not include the potential effect of obscuring circumnuclear dust, which cannot be easily estimated, or any other systematic effects such as deviations from axisymmetry that cannot be properly treated by our dynamical modeling method. These factors are discussed in detail in the following sections.

Pastorini et al. (2007) estimate the mass of the black hole in NGC 4258 using gas kinematics, but their 95% confidence intervals span a factor of ten in mass so this is not a strong test of the reliability of black-hole mass estimates.

For this work, we use 7.28 Mpc for the distance to NGC 4258 (Tonry et al. 2001), which is in excellent agreement with the maser-derived distance of 7.2 Mpc. At that distance,  $1'' \simeq 35$  pc.

In §2 we present the photometric and kinematic datasets, which consist of *HST* WFPC2 and NICMOS imaging and STIS spectroscopy, complemented by ground-based imaging and long-slit spectroscopy that extend data coverage to larger radii. We discuss the large-scale morphology of the galaxy in §3, mainly as it pertains to the determination of the contribution of the stars to the gravitational potential. In §4 we consider the consequences of the color

gradient in the central  $2''$ . §5 presents the dynamical models. We conclude in §6.

## 2. OBSERVATIONS AND REDUCTION

### 2.1. Photometry

Here we describe the acquisition and reduction of the photometric data, which are needed mainly to determine the stellar mass distribution and the kinematic tracer profile, in the way described in §5.1 and §5.4.

A journal of the imaging observations, from which the surface photometry was derived, is shown in Table 1. A wide variety of data are available in different colors, both from *HST* and from the ground. For reasons explained in §4.1, we produced three luminosity profiles. (i) The near-infrared (NIR) profile was created by combining ground-based and *HST* *J*, *H*, and *K*-band images, as described in §2.1.1. (ii) The *V*-band profile was generated from images in the *V* band (*HST*) and in the *R* band (ground-based), as described in §2.1.2. (iii) The *I*-band profile was created from the *HST* *I*-band image, as described in §2.1.2. Although this image was saturated in the nucleus, it was useful to consult for the luminosity weighting (normalization) of the line-of-sight velocity distributions (LOSVDs), as it identifies the kinematic tracer population (§5.4).

#### 2.1.1. Reduction of the *J*, *H*, and *K*-Band Data

The 2MASS *J*, *H*, and *K*-band images (Figure 1, top row) were kindly provided to us by Tom Jarrett (Jarrett et al. 2003), and extend out to  $R \approx 8'.6$  from the center<sup>1</sup>. For the morphological study of the large-scale properties of the galaxy (§3), the signal-to-noise ratio (S/N) was boosted by constructing a composite *J+H+K* image, which was then smoothed with a Gaussian point-spread function (PSF) having full width at half maximum (FWHM) of  $7''$  for  $r \leq 60''$  and  $\text{FWHM} = 11''$  for  $r > 60''$ . The 2MASS *K*-band image was reduced in a manner similar to that of the *J+H+K* image. It proved to have sufficiently high S/N to give a reasonably adequate measurement of the outer disk. A comparison of the *K*-band and *J+H+K*-band photometry provides an estimate of the uncertainties; these are dominated by the effects of patchy star formation and other irregularities, not by photon statistics.

---

<sup>1</sup>Throughout the paper, *R* refers to distance from the center of the galaxy, while *r* refers to distance along the isophotal semimajor axis.

Therefore, we decided to discard the  $J+H+K$ -band profile as a tracer of stellar mass in the dynamical modeling, and to use the  $K$ -band profile instead, as being less affected by these irregularities.

The KPNO 2.1-m telescope  $K$ -band image extends out to  $R \approx 3'$  from the center (Figure 1, bottom row). Comparison of the 2MASS  $K$ -band profile with the KPNO  $K$ -band profile, which has a higher spatial resolution, showed that the 2MASS profile is affected by smoothing only at  $r < 32''$ , so the 2MASS profile was truncated inside this radius. Thus, the KPNO profile was used for  $2'' < r < 32''$  and the 2MASS profile at  $r \geq 32''$ .

Chary et al. (2000) obtained *HST* NICMOS images of NGC 4258 in bandpasses that approximate  $J$ ,  $H$ , and  $K$ . Eric Becklin and Ranga Chary kindly made the reduced images available to us (Figure 2), along with the corresponding PSF images. Details of the reductions can be found in Chary et al. (2000). The *HST* WFPC2  $V$ -band image (§2.1.2) shows extensive dust at  $r \gtrsim 2''$  on the SW side of the center and a few thinner dust patches on the NE side. There is also a scatter of faint sources in the bulge, apparently associated with some ongoing star formation. In the NICMOS  $K$ -band image, these faint sources are not visible, and the dust patches on the NE side are essentially invisible as well. However, the dust on the SW side, although less conspicuous in  $K$  than in  $V$ , remains a substantial problem that we had to correct. After considering a number of alternatives, we chose the strategy of creating a symmetrized image of the galaxy, whereby the SW side was replaced with the NE side flipped (not rotated) across the major axis. As a check, the profiles from both the symmetrized and the unsymmetrized  $K$ -band image were compared and found to agree extremely well at  $r \lesssim 2''$ . Therefore, this symmetrization is not a factor in the  $V - K$  color gradient discussed in §4.1. We applied the same procedure to the  $J$ - and  $H$ -band images, as well.

The nucleus of NGC 4258 emits broad permitted lines (Ho et al. 1997), and is classified as a Type 1.9 Seyfert. The AGN at the center is very red (Chary et al. 2000) and, in the  $K$  band, it appears as a bright, unresolved point source that clobbers the central brightness distribution of the stars and needs to be subtracted. Unfortunately, the PSF provided by Chary et al. (2000) was determined using the TinyTim routine and not from actual images taken at the same time as the galaxy observations. It proves to be a mediocre match to the AGN at  $r < 0''.2$ , in the sense that there is a residual diffraction pattern no matter how the PSF is scaled. We applied the following procedure to improve the quality of the PSF subtraction (cf. Figure 3). Using VISTA (Lauer, Stover, & Terndrup 1983), we scaled the TinyTim PSF image by various factors and measured the resulting surface brightness profiles in the residual image using the unsymmetrized galaxy image. We also examined the residual images to see which ones had the small-scale structure, illustrated in the top left

image of Figure 3, optimally subtracted. Most of the weight in the choice of the final PSF scale factor came from how well the first diffraction ring of the AGN was subtracted. The scale factor that we finally adopted in this way yields ellipticity and position angle profiles that are both smooth and well behaved, which is reassuring. This is not the case with scale factors that differ by more than  $\pm 10\%$  from the adopted value. However, ultimately no value of the scale factor allows both a convincing subtraction of the first diffraction ring and a smooth profile at  $r < 0''.2$  that follows the power law seen at larger radii. This is probably a result of the imperfect match of the TinyTim-generated PSF to the  $K$ -band data. It is unlikely that a real galaxy feature is involved, considering that no such feature is detectable in the higher-resolution  $V$ -band image in the radial range  $0''.05 < r < 0''.2$  (cf. §2.1.2).

We also applied forty iterations of Lucy deconvolution (Lucy 1974; Richardson 1972) to the *HST* NICMOS  $J$ ,  $H$ , and  $K$ -band images using the PSFs from Chary et al. (2000). Because the PSFs are not ideal, we applied the deconvolution to images with the PSF of the AGN subtracted as explained above. Still, the deconvolved  $K$ -band image showed bad “ringing,” so we truncated it inside  $r = 0''.46$ . The  $J$ -band profile appeared better behaved, at least partly since the AGN is much dimmer at this bluer wavelength, although there was also some sign of a residual AGN at  $r < 0''.1$ . The  $J$ ,  $H$ , and  $K$ -band deconvolved profiles agree very well at  $r \gtrsim 0''.5$ , where the AGN is not a problem, and the ellipticity profiles are all well behaved.

Based on the preceding analysis, we decided (i) to use the original (not deconvolved)  $K$ -band photometry for  $r \geq 2''.8$  (KPNO data at  $2''.8 \leq r < 32''$ , and 2MASS data at  $32'' \leq r \leq 560''$ ), (ii) to average the deconvolved NICMOS  $K$ -band and  $J$ -band photometry for  $0''.2 \leq r < 2''.8$ , and (iii) to use deconvolved  $J$ -band data for  $0''.038 \leq r < 0''.2$  in order to avoid the AGN as much as possible. The resulting profile is shown in Figure 4. However, even in  $J$ , the points at  $r < 0''.11$  are probably still affected by the AGN. We elaborate on this point in §4.2.

### 2.1.2. Reduction of the $V$ and $I$ -Band Data

We used the MDM 1.3-m telescope to obtain an image of the galaxy in the  $R$  band (Figure 5). The image was reduced and dust-clipped in the usual way. The luminosity profile was then extracted and matched to the  $V$ -band *HST* profile, discussed below, in the range  $5'' \lesssim r \lesssim 7''$ , using a  $V$ -band zeropoint. There were no significant color, ellipticity, or position angle (PA) gradients between the  $V$ -band and  $R$ -band profiles over the radial range in which they were matched. Henceforth, we will refer to this composite profile, made by stitching together the *HST*  $V$ -band profile with the  $R$ -band profile shifted by a constant

offset, as the  $V$ -band profile. It extends out to  $r \approx 150''$ .

We obtained *HST* WFPC2 images of the NGC 4258 nucleus through the F547M filter under program GO–8591. The F547M filter was selected to exclude any bright emission lines associated with the AGN; it is roughly equivalent to a narrow  $V$ -band filter, and is referred to as such in the remainder of this paper. The galaxy was centered in the PC1 chip and dithered in a  $2 \times 2$  square raster of  $\sim 0.5$  pixel steps over four separate 400 s exposures to maximize the spatial resolution of the complete data set. The four dithered images were combined into a single Nyquist-sampled “super image” using the algorithm of Lauer (1999a), which provides for the optimal combination of undersampled images without any associated degradation of the resolution. This final image has a pixel scale of  $0''.0228$ , twice as fine as that of the original images. However, the Nyquist image remains modulated by the *HST* PSF; thus, it was deconvolved prior to further analysis using 80 iterations of the Lucy (1974) and Richardson (1972) algorithm. The PSF was estimated using the TinyTim package, but incorporates the WFPC2 pixel-response function recovered by Lauer (1999b). The final deconvolved  $V$ -band image of NGC 4258 is shown in Figure 6.

The  $V$ -band surface brightness profile of NGC 4258, shown in Figure 4, was estimated from the F547M Nyquist image using a combination of the high spatial resolution algorithm of Lauer (1985) and the least-squares estimator of Lauer (1986). The patchy dust seen throughout the bulge of NGC 4258 complicates measurement of the brightness profile; as is visible in Figure 6, there is a compact dust feature just slightly offset from the nuclear source that was especially problematic. For all dust features other than the central patch, pixels affected by dust could simply be excluded from the least-squares profile estimator. In practice, this was done iteratively by comparing the image to a model reconstructed from the profile to isolate faint dust absorption that may have been missed during the initial inspection of the image. Unfortunately, pixels could not be masked out of the high-resolution profile algorithm, which is used in preference to the least-squares estimator for  $r < 0''.5$ , so the nuclear dust patch was first filled in with an estimated correction provided by the lower-resolution least-squares algorithm. This initial correction was then refined by replacing it with an improved estimate provided by a model reconstructed by the high-resolution profile.

Figure 6 shows the central portion of the  $V$ -band image divided by a model reconstructed from the final brightness profile. Apart from the nuclear dust patch, the residuals are flat, showing that the brightness profile extracted is faithful to the central structure of NGC 4258. The nuclear dust patch, itself, is clearly compact, affecting only a single quadrant of the nucleus, which again allowed it to be isolated from the profile estimation. As a “sanity check” on the brightness profile, we compared the profile to an intensity trace taken along the bulge semimajor axis on the side of the nucleus opposite the nuclear dust patch. The



two measures agreed extremely well, showing that the final profile is not strongly affected by any residual dust features or the pixels excluded from the analysis.

In addition to the *HST* F547M data, we also analyzed two archival PC1 F791W (*I* band) images obtained by Cecil et al. (2000) under program GO–6563. Unfortunately, both images were saturated at  $r < 0''.09$  from the nucleus, and thus provide information only at somewhat larger radii. The images were combined and deconvolved; however, without a full accounting of the light contributed by the nucleus, the *I*-band profile should be regarded with caution for  $r < 0''.5$ .

Using the F547M and the F791W images, we created a F547M/F791W color map of the nuclear region of the galaxy, approximating  $V - I$  (Figure 7). The color map shows more clearly the distribution of dust in the center, and will be further discussed in §4.1. A larger-scale view of the central region of the galaxy is shown in Figure 8, which is a composite color image created by combining the F547M and the F791W images along with an archival F300W (*U*-band) image, also obtained by Cecil et al. (2000).

## 2.2. Spectroscopy

We used the Ca II triplet absorption line (8498 Å, 8542 Å, 8662 Å; hereafter CaT) to determine the stellar LOSVDs at the center of NGC 4258, and at various positions along the major axis (out to  $R = 18''.18$ ) as well as along the minor axis (out to  $R = 11''.69$ ). The spectra were obtained from the ground as well as with the *HST* Space Telescope Imaging Spectrograph (STIS). Spectrograph configurations are shown in Table 2.

In particular, we made 24 cosmic-ray-split exposures of NGC 4258 with STIS to obtain high-quality nucleus-centered CaT spectra along the major axis of the galaxy, out to  $R = 0''.80$ . The STIS slit was placed at PA = 140° instead of directly on the major axis (PA = 150°) because of guide-star constraints. Our reduction procedure closely followed that of Pinkney et al. (2003). The procedure bypasses the pipeline (“Calstis”) reduction so that we can employ “self-darks,” i.e., dark frames that are constructed by combining our dithered datasets with the galaxy light rejected. Our method works best if all of the exposures are taken within a short period of time because of the rapidly changing dark pattern on the STIS CCD. This was not quite the case here, since the exposures were taken on March 12 and 21, 2001. Nevertheless, a single self-dark worked well.

There is one small difference between our STIS reduction procedure and that described by Pinkney et al. (2003): the initial dark subtraction was done with an archival, “weekly” dark rather than by a sum of the galaxy frames with a region around the galaxy masked out.

This created a smoother dark on which to begin further iterations using the same “self-dark” strategy.

We also used the Modspec spectrograph on the MDM 2.4-m telescope to obtain ground-based CaT spectra along both the major and minor axes at larger radii. The configuration is again shown in Table 2. The seeing varied between  $1''$  and  $1''.5$  (FWHM). Kinematic parameters were extracted out to  $R = 18''.18$  and  $R = 11''.69$  along the major and minor axis, respectively. Again, the reduction procedure followed closely that described by Pinkney et al. (2003).

Figures 9 and 10 show spectra extracted at several radial positions from the STIS and the ground-based data, respectively. The emission-line feature visible near  $8620 \text{ \AA}$  (rest frame) in the nuclear STIS spectrum in Figure 9 is most probably the Fe II  $8618 \text{ \AA}$  line, and had to be removed before the LOSVD fitting could be done. Consequently, there was a concern that the central (or central few) LOSVDs would be less reliable, but it proved easy to interpolate under the line (see Figure 9), so in the end this was not a problem.

We decided to discard the central ground-based LOSVD along the major axis, because of concerns about template mismatch and AGN contamination. In retrospect, the central ground-based LOSVD on both the major and minor axes should have been dropped since the STIS data had comparable statistical quality and much better understood PSFs. In fact, we used the minor axis central LOSVD, except in one experiment, where its exclusion had no effect (see §5.3).

In a dust-free axisymmetric galaxy that also exhibits symmetry about the equatorial plane, such as assumed by our modeling method, kinematic quantities also manifest symmetries about the center. This entitles us to “symmetrize,” with respect to the center of the galaxy, the LOSVDs along the major and minor axes, for both STIS and Modspec. This process helps alleviate potential biases in the extraction of the velocity profile. Gebhardt et al. (2003) provide more details on how this was done. Unfortunately, NGC 4258 contains substantial quantities of dust, especially near the dynamically important central region (Figures 6, 7), which calls into question the validity of this assumption. Potential implications are discussed in §6.

We used the maximum penalized likelihood method (MPL), as described by Pinkney et al. (2003), to derive LOSVDs from all the CaT spectra. A nonparametric form of the LOSVDs, rather than Gauss-Hermite moments, was used for the dynamical modeling. Each LOSVD was represented by 13 equally spaced velocity bins, with the uncertainty in each bin determined from Monte Carlo simulations.

Figure 11 illustrates  $V$ ,  $\sigma$ ,  $H3$ , and  $H4$ , the fitting parameters from the truncated Gauss-

Hermite series expansions of the LOSVDs (Gerhard et al. 1993; van der Marel & Franx 1993), along the major and minor axes of the galaxy, both from STIS and from the ground. The same parameters in tabular form can be found in Table 3. We stress again that a nonparametric form of the LOSVDs was actually used for the dynamical modeling. We anticipate our best fitting model discussed in §5.1 by illustrating its projected Gauss-Hermite moments here.

### 3. THE LARGE-SCALE MORPHOLOGY

NGC 4258 is a typical oval-disk galaxy (Kormendy 1982), classified as SAB(s)bc. Morphologically, the disk consists of two nested regions of slowly varying surface brightness: the “inner oval” component ( $PA \simeq 156^\circ$ ) is much brighter than the “outer oval” component ( $PA \simeq 150^\circ$ ), and both have relatively sharp outer edges, at  $R \simeq 200''$  and  $R \simeq 560''$ , respectively (Figure 1). Embedded in the inner oval component is a bulge ( $PA \simeq 146^\circ$ ) which remains important out to  $r \simeq 40''$ , as well as a weak bar ( $PA \simeq 11^\circ$ ) extending out to  $R \simeq 150''$ . These components can also be identified using the profiles in Figure 4.

We are interested in the large-scale morphological properties of NGC 4258 primarily to establish that there are no major deviations from the assumption of axial symmetry, which is built into our modeling method (§5.1). Deviations from axisymmetry can be important for two reasons. First, orbits in a non-axisymmetric potential do not conserve any component of the angular momentum. Therefore, the orbital structure of a non-axisymmetric system can be considerably different from that of an axisymmetric one. Second, non-axisymmetric deviations can induce kinematic signatures in the radial velocity profile similar to those created by a central mass concentration. Either effect can bias a black hole mass estimate made under the assumption of axisymmetry.

The ellipticity profiles in  $V$  and in the NIR are quite different in the innermost  $0''.2$ , but they agree rather well further out. We consider the ellipticity profile in  $V$  to be overall more reliable than that in the NIR due to the higher resolution in  $V$ . It becomes progressively flatter from the center out to  $r \simeq 5''$ , and then it remains approximately constant between  $r \simeq 5''$  and  $12''$ . The ellipticity starts dropping again out to  $r \simeq 40''$ , but this is probably caused by the weak bar, which adds extra light in the minor-axis direction while probably having no effect on the major-axis profile. The onset of the dominance of the disk is signified by the increasing ellipticity outward of  $r \simeq 40''$ .

If we wanted to rigorously test these morphological characterizations, we would have to perform a full bulge-bar-disk photometric decomposition. However, such a decomposition

would be very uncertain because of parameter coupling: the bar is very weak, and trading light between the components while correspondingly changing their isophote shapes would provide considerable freedom to tinker with the bulge ellipticity.

In the absence of extinction, the projected isophotes of a galaxy that has emissivity constant on coaxial and similar spheroids (as assumed in our dynamical modeling) are concentric, coaxial, and similar ellipses (Contopoulos 1956; Fish 1961). The absence of any strong isophote twists out to  $r \simeq 40''$ , the beginning of the weak bar, indicates that, to a good approximation, NGC 4258 is axisymmetric out to that radius. Furthermore, the fact that the PA of the bulge and of the outer disk agree quite well is evidence against a triaxial bulge. However, there *does* exist a strong isophote twist between  $40''$  and  $150''$ , caused by the bar, while Figure 11 shows some minor-axis rotation in the bulge, outside  $R \simeq 10''$ , which could be indicative of triaxiality at intermediate radii.

Even though our current algorithm cannot model triaxial components, the dynamical effect of the bar on the measured value of the black hole mass is probably small, for at least three reasons: (i)  $M_\bullet$  is mostly determined from the dynamics near the center, where triaxial deviations are least significant; (ii) bars generally have relatively little effect on the kinematics — for example, even the much stronger bar of NGC 936 has little effect on the velocity dispersion of that galaxy (Kormendy 1983, 1984); (iii) and finally the velocities of bar stars that cross the slit, while probably somewhat bigger than the local circular velocity (a  $\sim 5$ – $10\%$  effect), are seen moving nearly perpendicular to the line-of-sight because the bar is strongly inclined to the major axis, and hence they probably do not significantly affect the observed kinematics.

In summary, NGC 4258 contains non-axisymmetric structures which probably *do* affect the kinematics, and hence the black hole mass estimate, but probably only in a minor way.

#### 4. VARIATIONS IN $M/L$ RATIO

Stellar population gradients, dust extinction, and contamination by an AGN can all induce variations in the  $M/L$  ratio, which have to be taken into account when deriving the stellar mass density profile from the luminosity density profile. We first discuss variations in  $M/L$  far from the AGN-dominated nuclear region, and then we describe the complications due to the AGN.

#### 4.1. The Stellar $M/L$ Ratio Far from the AGN Point Source

Color gradients in the outer disk of NGC 4258 are small, even between the  $R$  and  $K$  bands (Figure 4), implying that the  $M/L$  ratio in the disk is not seriously affected by star formation or dust. However, inside  $\sim 2''$  from the nucleus, the  $V$ -band profile “peels off” from the NIR profile and becomes flatter. This color gradient can be seen in Figure 4, but becomes more apparent in Figure 12 which shows the inner  $10''$  of the surface brightness profile. Also, the color map shown in Figure 7 clearly identifies the color gradient as a “red,” diffuse area surrounding the nucleus out to  $r \approx 2''$  ( $R \approx 1'' - 2''$ ). This is an issue for the dynamical modeling because it takes place in the dynamically important central region, which affects the entire model: we must determine which, if either, of the two profiles ( $V$ -band or NIR) traces stellar mass.

Could the color gradient be caused by variations in the stellar population? The strongest evidence *against* variations in the stellar population is the absence of any marked color gradient between the  $J$  and  $K$  profiles, which should be present if the central NIR brightening were caused by either a metallicity gradient or red supergiant stars. Furthermore, although some traces of scattered star formation can be seen on the  $V$ -band image (Figure 6) as well as on the color map (Figure 7), they are absent in the NIR images (Figure 2), even after accounting for the different FWHM of the PSFs.

More information can be obtained from the equivalent width (EW) profiles of the three CaT line components, which we computed from the STIS spectra extending out to  $1''.5$  from the center (Figure 13). A decreasing EW profile would be evidence of a young stellar population or of a brightening  $I$ -band nonthermal continuum. A drop is seen in the central  $0''.3$ , and is discussed in the next subsection. Here we are concerned with possible trends beyond that radius. For  $r > 0''.3$ , there is a hint of a slow increase in the EW away from the center, but the data are also consistent with a flat profile. However, the datapoints at  $r > 0''.8$  suffer from the low S/N of the originating spectra, and we have no data as far out as  $\sim 2''$ , where the  $V$ -band profile begins to peel off.

The other possible explanation is the presence of diffuse dust, which would produce a small gradient in  $J - K$  but a larger one in  $V - J$ , just as observed. The observed smoothness in the  $V - J$  color gradient would then imply a similarly smooth increase in the projected density of diffuse dust toward the center.

In the end, we were unable to determine unequivocally whether the origin of the color gradient is a variation in the stellar population or the presence of a diffuse dust component. We decided to construct models for both of these possibilities, and investigate the uncertainties induced on the black hole mass (§5.4).

#### 4.2. The Stellar $M/L$ Ratio Near the AGN Point Source

Dynamical modeling only strongly constrains the *total* mass,  $M_{\text{tot}}(r_0) = M_{\bullet} + M_{*}(r_0)$ , inside a small radius  $r_0$  around the center, where  $M_{*}(r_0)$  is the enclosed stellar mass, and  $r_0$  is comparable to the spatial resolution of the nuclear spectrum ( $\sim 0''.1$ ). Therefore, there is a degeneracy between  $M_{\bullet}$  and  $M_{*}(r_0)$ , which can be resolved only if we know  $M_{*}(r_0)$  separately, i.e., only if we know the luminosity profile and the stellar  $M/L$  ratio inside  $r_0$ . The latter is assumed to be constant throughout the galaxy and is predominantly constrained by the dynamical model at large radii (§5.1). In essence,  $M_{\bullet} = M_{\text{tot}}(r_0) - M_{*}(r_0)$  corresponds to the “excess” dynamical mass inside  $r_0$  after subtraction of the mass due to stars. Therefore, we must again determine which, if either, of the two luminosity profiles ( $V$  band or NIR) traces stellar mass,  $M_{*}$ .

The  $V$ -band profile, which is well determined down to  $r \simeq 0''.011$ , manifests a progressively more shallow slope for  $r \lesssim 0''.15$ , interrupted by a peak within  $0''.04$  of the nucleus. Although the cause of the peak is not entirely clear, it is unlikely that it is due to light from an old stellar population. The CaT EW profile (Figure 13) shows a  $\sim 30\%$  decline within  $0''.2$  of the nucleus, which strongly suggests contamination by a continuum source, possibly OB stars or a nonthermal AGN.

Notwithstanding the uncertain origin of the peak, it seems unlikely that it traces stellar mass. Therefore, we replaced the innermost three  $V$ -band datapoints in a way that extrapolates inward the profile at  $0''.04 \lesssim r \lesssim 0''.15$  (Figure 12; §5.4). However, we also created models *with* the central peak, to investigate its effect on  $M_{\bullet}$ . Not surprisingly, the effect was negligible because the light in the peak corresponds to a very small mass (§5.4).

In §2.1.1 we saw that, at  $r \lesssim 0''.11$ , the  $J$ -band profile begins to show signs of contamination by AGN light, and the PSF of the AGN could not be subtracted reliably. We also saw earlier that the central depression in the CaT EW profile begins at  $r \simeq 0''.2$ , and implies a brightening of the CaT continuum, which lies in the  $I$  band, inside that radius. The AGN is red, so it seems likely that the  $J$ -band profile is even more affected by the AGN continuum radiation than the  $I$ -band profile. While luminous AGNs normally have a blue featureless continuum, low-luminosity AGNs such as NGC 4258 tend to have emission spectra that peak in the mid-infrared (Ho 1999), probably as a consequence of their low accretion rates (Ho 2008). Taking all these considerations into account, we decided that the  $J$ -band profile inward of  $r \simeq 0''.2$  cannot be trusted to trace mass (i.e., the old stellar population). Accordingly, inside  $r \simeq 0''.2$  we replaced it with a profile that follows the  $V$ -band profile *without* the central peak. As explained above, this profile is presumably not affected by the AGN. The related dynamical models are discussed in §5.4.

## 5. DYNAMICAL MODELING

### 5.1. The Method

A detailed account of our dynamical modeling method is provided in the Appendix. Here we present a short description with emphasis on NGC 4258.

The first step involves a deprojection of the surface photometry to obtain the three-dimensional luminosity density. This is done under the assumption that emissivity is constant on similar, coaxial spheroids. The deprojection is performed via a nonparametric Abel inversion (cf. Gebhardt et al. 1996) assuming a value for the inclination angle ( $i = 72^\circ$  in the base model). The gravitational potential can then be recovered by specifying a central point mass (“black hole”)  $M_\bullet$  and the stellar  $M/L$  ratio,  $\Upsilon$ , assumed constant throughout the galaxy. The dynamical models for NGC 4258 extend out to  $r = 100''$ .

The dynamical models are constructed for a grid of  $(M_\bullet, \Upsilon)$  values. Each model consists of a superposition of representative orbits, appropriately weighted to match the observed kinematics, subject to constraints that force the stellar density distribution to match the luminous density distribution of the galaxy. Each model is computed using  $N_o \approx 7000$  orbits. Orbits are integrated for about 100 crossing times.

Self-consistency is enforced by requiring that the model satisfy exactly the photometric constraints on a polar grid of 15 radial shells as described in the appendix, each subdivided into 4 bins in polar angle. The grid used to solve Poisson’s equation is 4X finer than the grid used to bin the kinematic results. For most orbits energy is conserved to much better than 1%.

For each model, the orbit weights that best fit the observed kinematics are determined by minimizing

$$\chi^2 = \sum_k \left[ l_{k,o} - \sum m_{ik} w_i \right] / \sigma_k^2, \quad (1)$$

where  $l_{k,o}$  is the light at a specific position and velocity (the index  $k$  runs over both position and velocity) with uncertainty  $\sigma_k$ , and where  $m_{ik}$  is the mass deposited by the  $i^{th}$  orbit weighted by  $w_i$  in the  $k^{th}$  projected position and velocity bin; cf. §2.2). We use a maximum-entropy technique as described in the Appendix to minimize  $\chi^2$  using non-negative orbit occupation numbers.

For each dataset, we determine  $\chi^2(M_\bullet, \Upsilon)$ . The minimum determines the best (most probable) combination of  $M_\bullet$  and  $\Upsilon$  for the galaxy. The  $\Delta\chi^2 = 1$  contour on the  $(M_\bullet, \Upsilon)$  plane, where  $\Delta\chi^2 \equiv \chi^2 - \chi_{\min}^2$ , determines the nominal “ $1\sigma$ ” uncertainty ranges for  $M_\bullet$  and  $\Upsilon$ .

The process of converting observational quantities to model input entails assumptions and systematic uncertainties that have to be taken into account when determining the uncertainty of the “best”  $M_\bullet$ , which may be larger than the nominal “ $1\sigma$ ” confidence band on the  $(M_\bullet, \Upsilon)$  plane. Therefore, the previous steps must be repeated for a number of plausible parameter choices (other than  $M_\bullet$  and  $\Upsilon$ ) in order to determine the overall uncertainty. We cannot afford to make an exhaustive exploration of the parameter space because of the time required to create the models. Instead, we opt to construct a base model corresponding to our “best guess” for the parameter values and investigate the effect on  $M_\bullet$  of varying each parameter independently.

The results from the dynamical modeling are summarized in Table 4, and the corresponding  $\chi^2$  contour maps are shown in Figure 14. The black hole mass for the base model, which uses the  $V$ -band profile *without* the central peak for both the mass and the kinematic tracer profiles, is  $M_\bullet = 3.31^{+0.22}_{-0.17} \times 10^7 M_\odot$  with a total (*not* per degree of freedom)  $\chi^2_{\min} \approx 290$ .

The total number of parameters is 27 (LOSVDs) times 13 (velocity bins), which is 351. Typically, the reduced  $\chi^2$  is 0.3 to 0.5 in our models (Gebhardt et al. 2003), which is less than the expected value of unity because of covariance in the LOSVD components. For NGC 4258, the reduced  $\chi^2$  is near unity, but most of the contribution to  $\chi^2$  comes from the minor axis. The velocity centroid on the minor axis varies much more than the stated uncertainties (see Figure 11), whereas an axisymmetric model would have zero velocity along the minor axis. Regardless of whether this contribution is due to underestimated uncertainties or real non-axisymmetric motion, it is the main cause for the inflated  $\chi^2$ . Along the major axis, the reduced  $\chi^2$  is about 0.4, which is typical for the orbit-based models.

## 5.2. Ambiguities in the Deprojection Parameters

### 5.2.1. Isophotal Ellipticity ( $\epsilon$ )

The (projected) ellipticity profile of NGC 4258 is discussed in §3. The profile varies with radius, but the origin of the variation (disk, weak bar, genuine variations in the axis ratios of the bulge isodensity spheroids) is not clear. Therefore, although it is possible to incorporate an arbitrary ellipticity profile  $\epsilon(r)$  in our modeling algorithm, we preferred instead to make models with a constant ellipticity profile, and examine the extent to which  $M_\bullet$  is affected by the adopted value.

For the base model we used  $\epsilon = 0.35$ , corresponding to the mean ellipticity in the radial range  $2'' \lesssim r \lesssim 65''$ . The effect of varying  $\epsilon$  was examined in model D1, for which we used  $\epsilon = 0.45$ . We obtain  $M_\bullet = 3.48^{+0.42}_{-0.38} \times 10^7 M_\odot$ , a slightly higher mass but within the same



“ $1\sigma$ ” confidence as the base model.

Nonetheless, the assumption of constant ellipticity is clearly problematic because the ellipticity profile varies between  $\sim 0.1$  and  $\sim 0.6$ .

### 5.2.2. Disk Inclination Angle ( $i$ )

We need to know the inclination of the disk to deduce the intrinsic ellipticity of the isophotes from their projected ellipticity, under the assumption that the equatorial plane of the bulge of the galaxy is coplanar with the galactic disk.

The outer disk (beyond  $r \approx 200''$ ) has average and maximum ellipticities of  $\epsilon = 0.62$  and  $0.64$ , respectively. If this disk is infinitesimally thin, the corresponding inclination angles are  $i = 69^\circ$  and  $70^\circ$ , respectively, where edge-on corresponds to  $i = 90^\circ$ . If this disk were thick with an intrinsic axis ratio of  $0.25$  (Sandage, Freeman, & Stokes 1970), then the corresponding inclinations would be  $i = 73^\circ$  and  $75^\circ$ , respectively. At large radii, the optical PA is  $150^\circ$ . Van Albada (1980), using H I kinematic observations, derives the same PA and  $i = 72^\circ$ , which is consistent with the photometrically derived inclination given the uncertainty in the intrinsic thickness of the disk.

We therefore adopted  $i = 72^\circ$  for the base model, but we also examined the sensitivity of  $M_\bullet$  to variations in  $i$ . Model D2 is identical to the base model except  $i = 62^\circ$ , a value close to the lowest inclination angles that we found in the literature. We obtained a  $\sim 10\%$  higher mass,  $M_\bullet = 3.62^{+0.38}_{-0.49} \times 10^7 M_\odot$  which is consistent with a  $M_\bullet \propto (\sin i)^{-1}$  dependence. This would be expected in a rotationally supported system. It appears from our models that the inner part of the galaxy is rotating quite rapidly. For this model,  $\chi^2_{\min} = 303$ , which is greater than  $280$ , the  $\chi^2_{\min}$  for the base model. This could be interpreted as evidence that the base model is more likely to be true, at least within the framework of assumptions of the modeling method.

We did not attempt to obtain a better estimate for the errors due to deprojection (by running models for more combinations of  $i$  and  $\epsilon$ ) because the uncertainties in the luminosity profiles (§5.4) dominate the errors.

## 5.3. Ambiguities in the Kinematic Data

In §2.2 we mentioned that the presence of an emission line near the CaT in the nuclear STIS spectrum may have affected the reliability of the LOSVD extraction. In fact, the next

two STIS spectra (at  $R = 0''.05$  and  $0''.10$ ) show (weaker) signatures of the same emission line, as well. We also mentioned that we have some concerns about the quality of the central LOSVD along the minor axis, in the ground-based data. In this section we remove the suspect LOSVDs from the  $\chi^2$  fit, and examine the effect on  $M_\bullet$ .

In models K1 and K2 we isolate the uncertainty introduced to  $M_\bullet$  by the potentially unreliable LOSVD extraction. Model K1 is identical to the base model, except the nuclear STIS LOSVD is not included as a constraint. In model K2, the three innermost STIS LOSVDs are not included. In model K1, the effect on  $M_\bullet$  is very small. This is reassuring, since it is the nuclear spectrum that would have been affected the most. Model K2 yields a significantly lower  $M_\bullet = 2.20_{-0.31}^{+0.54} \times 10^7 M_\odot$  but with a much higher uncertainty, which overlaps with the base model at the  $\sim 1.5\sigma$  level.

An interesting question is whether *HST* spectroscopy is required to find evidence for a black hole. Using ground-based kinematic data alone should, of course, yield a black hole mass consistent with the mass obtained by also including *HST* data, albeit with larger uncertainties, depending primarily on the angular size of the radius of influence of the black hole on the sky. We address this question for NGC 4258 with model K3, which is identical to the base model, except only ground-based kinematic data are used. It turns out that the stellar  $M/L$  ratio can be constrained quite well, but the black hole mass,  $M_\bullet = 1.03_{-0.28}^{+1.00} \times 10^7 M_\odot$ , is very uncertain. This is not surprising, considering that the radius of influence for the black hole in the base model is  $GM_\bullet/\sigma_e^2 \approx 0''.32$ , where  $\sigma_e = 105 \text{ km s}^{-1}$  is the velocity dispersion in the main body of the bulge. This is substantially smaller than the spatial resolution of the ground-based kinematic data, for which  $\text{FWHM} = 1''\text{--}1''.5$ . Therefore, *HST* kinematic data are critical for a well-constrained estimate of the black hole mass in this galaxy. *HST* photometric data are also critical for galaxies where the luminosity profile near the center cannot be reliably extrapolated from the profile farther out, as is also the case with this galaxy (unfortunately, it is still not possible to determine unambiguously the inner mass profile, as discussed in §5.4).

We also constructed model K4, which uses all kinematic data (STIS+Modspec) except the central ground-based LOSVD along the minor axis (the central ground-based LOSVD along the major axis was not included in *any* model). We find that  $M_\bullet$  is essentially identical to that of the base model.

#### 5.4. Ambiguities in the Mass and Kinematic Tracer Profiles

In §4 we saw that stellar population gradients and/or dust extinction in the innermost  $\sim 2''$  of the galaxy, as well as light from the unresolved AGN, can induce variations in the measured stellar  $M/L$  ratio near the center of the galaxy. These have to be taken into account to determine which, if any, of the available luminosity profiles traces the mass density profile, and which, if any, corresponds to the luminosity profile of the kinematic tracer population. The latter profile is needed for the luminosity weighting (normalization) of the LOSVDs. Unfortunately, we were unable to make these determinations convincingly, for the reasons explained in §4.

Consequently, we decided to identify three possible luminosity profiles, and to make models that use them as either mass or kinematic tracer profiles. The expectation is that these three profiles correspond to limiting cases, and that the true profiles lie somewhere in between. Then, the spread in  $M_\bullet$  that we obtain from these limiting cases would be a good indication of the  $M_\bullet$  uncertainty caused by our inability to determine the true profiles.

The profiles, which are depicted in Figure 12, are the following:

- (1) *The  $V$  profile*: This is identical to the  $V$ -band profile as measured.
- (2) *The  $V_{\text{corr}}$  profile*: This is identical to the  $V$  profile, with the three innermost points replaced by a shallower core, as explained in §4.2.
- (3) *The  $\text{NIR}_{\text{corr}}$  profile*: For  $r > 0''.2$ , this is identical to the spliced  $J$ ,  $J+K$ , and  $K$  profiles in the top panel of Figure 4. Inward of  $0''.2$ , that profile is replaced by one that parallels (shows no color gradient with respect to) the  $V_{\text{corr}}$  profile, for the reasons mentioned in §4.2.

If the observed color gradient is mostly or entirely due to the presence of diffuse dust or metallicity, then the  $\text{NIR}_{\text{corr}}$  profile is a better tracer of mass than the  $V$  or the  $V_{\text{corr}}$  profiles. However, the  $V$ -band profile has higher intrinsic resolution and a dimmer AGN, and the WFPC2 is better understood photometrically than NICMOS. For these reasons, we try all three versions as stellar mass profiles.

The kinematic tracer population was observed in the CaT wavelength, which lies in the  $I$  band. It would thus be natural to use the  $I$ -band profile as the kinematic tracer profile. However, we saw in §2.1.2 that the  $I$ -band image is saturated in the central  $0''.09$ , and thus cannot be deconvolved. The NIR profile shares the same slope with the  $I$ -band profile at larger radii (where  $I$  is not saturated), and could arguably be used instead. Unfortunately, it is also ill-determined near the center due to the AGN and reduced resolution (§4.1). Consequently, we decided to again test both  $\text{NIR}_{\text{corr}}$  and  $V_{\text{corr}}$  as the kinematic tracer profile,

and examine the induced uncertainty in  $M_\bullet$ . For the base model we adopted  $V_{\text{corr}}$  because of its higher resolution and smaller AGN contamination. This is somewhat arbitrary, but the choice of the kinematic tracer profile turns out to have a very small effect on  $M_\bullet$ , as we will see below.

These scenarios were tested in models P1 through P4. Models P1–P3 substitute  $\text{NIR}_{\text{corr}}$  for  $V_{\text{corr}}$  in the mass and/or kinematic tracer profiles, and show that the choice of the stellar mass profile matters much more than the choice of the tracer profile. When  $V_{\text{corr}}$  is used for the mass profile (base model and P2),  $M_\bullet = 3.31^{+0.22}_{-0.17} \times 10^7 M_\odot$  or  $M_\bullet = 3.33^{+0.18}_{-0.17} \times 10^7 M_\odot$ , depending on whether  $V_{\text{corr}}$  or  $\text{NIR}_{\text{corr}}$  is used, respectively, for the tracer profile. These numbers become  $2.49^{+0.09}_{-0.10} \times 10^7 M_\odot$  and  $2.43^{+0.21}_{-0.30} \times 10^7 M_\odot$ , respectively, when  $\text{NIR}_{\text{corr}}$  is used for the mass profile (models P1 and P3). The relative insensitivity to the choice of the tracer profile is not surprising, considering that, e.g., for a spherical system, the tracer profile  $\nu(r)$  affects mass  $M(r)$  within radius  $r$  only via  $d \ln \nu / d \ln r$ , which by construction is nearly identical for both  $V_{\text{corr}}$  and  $\text{NIR}_{\text{corr}}$  near the center of the galaxy.

Model P4 substitutes  $V$  for  $V_{\text{corr}}$  in the mass profile. It yields  $M_\bullet = 3.25^{+0.22}_{-0.14} \times 10^7 M_\odot$ , very similar to the base model, reflecting the fact that the only difference between P4 and the base model is the small luminosity excess within  $0''.04$  of the nucleus, well below the spatial resolution of the kinematic data ( $\sim 0''.1$ ). The stellar  $M/L$  ratio is constrained at larger radii, so that the only difference in the stellar mass profile,  $M_*(r)$ , between P4 and the base model is due to this small luminosity excess. From the  $M_\bullet - M_*(r_0)$  degeneracy, discussed in §4.2, the only option for the modeling algorithm is to reduce  $M_\bullet$  by a (small) amount equal to the difference in stellar mass inside  $r_0 \approx 0''.1$  between P4 and the base model.

This point is illustrated in Figure 16, which shows the stellar mass profile,  $M_*(r)$ , and the total mass profile,  $M_\bullet + M_*(r)$ , for the base model and for models P1 and P4. The mass profiles of these models correspond to the three profile choices ( $V_{\text{corr}}$ ,  $\text{NIR}_{\text{corr}}$ , and  $V$ , respectively) discussed above. It is clear that dynamic modeling assigns black hole masses to P4 and to the base model such that they both contain the same total mass inside  $r \simeq 0''.04$  (since both models are constrained by the same kinematic data and the same  $V$ -band mass profile beyond  $r \simeq 0''.04$ ). This is not the case with model P1 which, although again constrained by the same kinematic dataset, is characterized by a different mass profile ( $\text{NIR}_{\text{corr}}$ ) outside of  $\sim 0''.1$ , the spatial resolution of the kinematic data.

## 6. DISCUSSION

The determination of the central black hole mass in NGC 4258 from stellar dynamics proved harder than anticipated. The main source of difficulty (and uncertainty in  $M_{\bullet}$ ) comes from the presence of a  $V - J$  color gradient in the central  $\sim 2''$  of the galaxy, which prevents us from determining the stellar mass profile near the center with confidence. The model that we trust most (“base model” in Table 4) yields  $M_{\bullet} = 3.31^{+0.22}_{-0.17} \times 10^7 M_{\odot}$  and assumes that the stellar mass is traced by the “corrected”  $V$ -band profile, or  $V_{\text{corr}}$  (Figure 12). This is identical to the  $V$ -band profile except for the removal of a small luminous “bump” in the central  $\sim 0''.04$ , which we attribute to the AGN. Using the uncorrected  $V$ -band profile yields a very similar  $M_{\bullet} = 3.25^{+0.22}_{-0.14} \times 10^7 M_{\odot}$  (model P4 in Table 4). This small black hole mass “deficit,” compared to the base model, corresponds approximately to the mass of stars in the luminosity “bump” and is a consequence of the degeneracy between stellar mass and black hole mass very near the center (§4.2; Figure 16).

Using the steeper  $J$ -band (NIR) profile as the mass tracer (model P1), we obtain  $M_{\bullet} = 2.49^{+0.09}_{-0.10} \times 10^7 M_{\odot}$ , a factor of 25% lower than in the base case. Although  $V$ -band light is more likely to be compromised as an indicator of the stellar mass distribution than  $J$ -band light, due to extinction and metallicity gradients, we have greater confidence in the base model because (i) the  $V$ -band profile is better determined near the center owing to the higher resolution of the  $V$  images, (ii) the AGN is considerably fainter in  $V$  than in  $J$ , making it easier to subtract, and (iii) the minimum  $\chi^2$  for the base model is 280, significantly less than the minimum  $\chi^2$  for the P1 model using  $J$ -band data (which was 303).

The spread in  $M_{\bullet}$  introduced by uncertainties in the deprojection parameters (models D1 and D2) is only of order 10%, so it is the uncertainties in the stellar mass profile that dominate the errors.

After all these sources of error are taken into account, our black hole mass determination is  $\sim 15\%$  lower than the “preferred” maser determination  $[(3.82 \pm 0.01) \times 10^7 M_{\odot}]$  and only 7% lower than the lowest maser determination  $[(3.59 \pm 0.01) \times 10^7 M_{\odot}]$  (rescaled to our distance for the galaxy). We view this level of agreement ( $2\sigma$ ) as evidence that stellar dynamical mass determinations using similar methods to those in this paper, and with data of comparable quality, are accurate at the  $2\sigma$  level or better. Our previous work has sought to avoid galaxies with dusty centers such as NGC 4258. In this case obscuration of high-velocity stars by the compact nuclear dust patch (§2.1.2), possibly associated with the masing disk, could be responsible for an underestimate of the black hole mass in our work. To these problems should be added possible systematic effects due to deviations from axisymmetry, which cannot be properly treated by our axisymmetric modeling code. We also note that the discrepancy between the mass determination from stellar dynamics and the maser mass

determination in NGC 4258 is smaller than the discrepancy between the stellar dynamical mass determination and the mass determination from individual orbits for our own Galaxy, which amounts to about a factor of two (Chakrabarty & Saha 2001; Ghez et al. 2005). Most concerns about black hole mass estimates from stellar dynamics have stressed the likelihood that the masses are overestimated, whereas here the stellar dynamical mass is smaller than the maser mass.

Finally, although we regard the maser mass in NGC 4258 as the gold standard in black hole masses, it is conceivable, however unlikely, that some unrecognized effect has led to an overestimate of the mass determined from maser kinematics.

We are grateful to Eric Becklin and Ranga Chary for providing the *HST* NICMOS images, and to Tom Jarrett for providing the 2MASS images before publication. We thank the referee, Tim de Zeeuw, for comments that improved the manuscript. C. S. is grateful to Seppo Laine and Ranga Chary for useful discussions. Support for proposal GO-8591 was provided by the National Aeronautics and Space Administration (NASA) through a grant from the Space Telescope Science Institute, which is operated by the Association of Universities for Research in Astronomy, Inc., under NASA contract NAS 5-26555. Support for this research was also provided by NASA grant NAG 5-8238 to the University of Michigan. A.V.F. is grateful for the support of NSF grant AST-0607485. This research has made use of the NASA/IPAC Extragalactic Database (NED) which is operated by the Jet Propulsion Laboratory, California Institute of Technology, under contract with NASA.

## A. Description of the Orbit-Superposition Method

For over two decades, orbit-superposition methods have been used to study the dynamics of galaxies. Originally invented to construct a model of a triaxial galaxy (Schwarzschild 1979), the methods have become the tool of choice for interpreting data in terms of equilibrium galaxy models. The most important feature of orbit-superposition models is that they provide a constructive proof that a given set of photometric and kinematic data can (or cannot) be reproduced by an equilibrium stellar system in a specified gravitational field. The computer code described in this appendix has been used to estimate black hole masses in galaxies (Gebhardt et al. 2003) and to determine the relative contributions of dark and luminous matter in elliptical galaxies (Thomas et al. 2004, 2005). It is a descendant of the spherical program described in Richstone & Tremaine (1988), but improved in two major respects: it treats the galaxy as axisymmetric rather than spherical, and it matches the full LOSVD of the galaxy at specified positions on the sky, rather than the second moment only.

Similar programs have been developed by van der Marel et al. (1998), Cretton et al. (1999), and Valluri et al. (2004).

A number of preliminary steps must be taken to convert the reduced data into inputs for the orbit-superposition method. These include the deprojection of the observed surface brightness to construct a light distribution in three-dimensional space and the reduction of spectra at different locations on the sky to projected velocity distributions. Both of these activities require additional assumptions or choices. We normally deproject under the assumption that level surfaces in stellar density are coaxial spheroids (Gebhardt et al. 1996) and we normally use a penalized maximum-likelihood estimator to construct the LOSVDs (Gebhardt et al. 2000a; Pinkney et al. 2003). Next we compute the gravitational field from the three-dimensional light distribution under the assumption that the mass consists of a black hole of mass  $M_\bullet$  and stars having a  $M/L$  ratio independent of position. Dark matter can be incorporated into such a model, but we have not done so here.

Once the preliminaries are complete, the calculation of a dynamical model by this method consists of two steps. First, a library of orbits is constructed using initial conditions that cover all possible locations in phase space. Each orbit’s contribution to the surface brightness and projected velocities is logged. Second, the orbits are combined to match the light distribution and LOSVDs of the galaxy as well as possible (using  $\chi^2$  parameter to assess the goodness of fit). This procedure is repeated for a set of black hole masses, and limits on the latter are set from  $\chi^2$  as a function of  $M_\bullet$ . Note that although different orbit libraries are required for each different ratio of  $M/L$  to  $M_\bullet$ , a single library can be used for various values of  $M_\bullet$  so long as  $M/L$  scales with  $M_\bullet$ .

### A.1. The Orbit Library

We construct the model on a grid in coordinates  $r, \eta$  where  $r$  is the radius and  $\eta$  is the latitude. We restrict ourselves to potentials (and mass distributions) symmetric about the equator. The grid is evenly spaced in  $\nu = \sin(\eta)$  from  $\nu = 0$  to 1, and in  $r$  in even intervals in  $k$  defined by

$$k = \frac{1}{a} \log \left( 1 + \frac{a}{b} r \right). \quad (\text{A1})$$

Bins in  $(r, \eta)$  are bounded by the grid points. Below we also use standard cylindrical coordinates  $(\varpi, z)$ . It is essential to explore the phase space of orbits with a resolution at least as fine as the resolution used to construct the models.

Orbits in axisymmetric potentials always have two isolating integrals, the energy  $E$ , and the  $z$ -axis angular momentum  $J_z$ . Regardless of the possible presence of a third integral,

conservation of  $E$  and  $J_z$  confine the orbit within a region of  $(\varpi, z)$  space defined by a boundary where the orbits' velocities are zero:

$$\Phi(\varpi, z) + \frac{J_z^2}{2\varpi^2} < E. \quad (\text{A2})$$

The allowed volume intersects the equator only over a limited range in radius with an upper and lower limit. We choose  $(E, J_z)$  pairs so that there is an orbit with upper and lower limits in the middle of each radial bin. We associate an area with each grid point  $(\Delta E \times \Delta J_z)$  by halving the distance to adjacent grid points. For each specified  $(E, J_z)$ , the section of allowed phase space (we ignore  $\phi$  because of the conservation of  $J_z$ ) that lies on the equator is a two-dimensional surface with coordinates  $\varpi$  and  $v_\varpi$  (a surface of section). A regular orbit is defined by a curve on this surface. We systematically tile this surface in the manner invented by Thomas et al. (2004), launching an orbit from the center of each bin and assigning a phase space volume to each orbit by

$$\Delta\Omega = \Delta E \Delta J_z \int T(\varpi, v_\varpi) d\varpi \times dv_\varpi, \quad (\text{A3})$$

based on the work of Binney, Gerhard, & Hut (1985), where  $T$  is the time between successive crossings of the equatorial plane.

The procedure above gives a starting position for each orbit in the equatorial plane of the model with a well-defined  $\varpi$ ,  $v_\varpi$ ,  $E$ , and  $J_z$ . We use  $E$  to determine  $v_z$ , and we integrate the motion of the orbit in the  $(\varpi, z)$  plane. Assuming that all orbits cross the equator, it is a complete survey of orbits. We follow the orbits of stars in spherical coordinates, to take advantage of the near sphericity of the mass distribution in the region where a black hole may dominate the gravitational field. Using  $r$  as the radial coordinate,  $\eta$  as the equatorial angle, and  $\phi$  as the axial angle, the equations of motion are

$$\frac{dv_r}{dt} = \frac{v_\eta^2 + v_\phi^2}{r} - \frac{\partial\Phi}{\partial r}, \quad (\text{A4})$$

$$\frac{dv_\eta}{dt} = -\frac{v_r v_\eta}{r} - \tan\eta \frac{v_\phi^2}{r} - \frac{1}{r} \frac{\partial\Phi}{\partial\eta}, \text{ and} \quad (\text{A5})$$

$$v_\phi = \frac{l_z}{r \cos\eta}. \quad (\text{A6})$$

The first two equations are integrated using a standard fourth-order Runge-Kutta method with variable timestep, and  $v_\phi$  is recovered at each timestep from equation (A6). We obtained good energy conservation by letting  $dt = \epsilon r / v_{\text{circ}}(r)$ , where  $v_{\text{circ}}$  is the velocity of a circular orbit at that radius, with  $\epsilon$  between 0.01 and 0.1. Orbits are followed for about



100 crossing times. We terminate the calculation of an orbit if its energy error exceeds 1%. Typical energy errors are 0.1%. The potential is set equal to zero at  $\infty$ .

The accelerations for the orbit integrations are determined by decomposing the assumed galaxy density distribution in spherical harmonics. Specializing immediately to axisymmetry gives

$$\Phi(\mathbf{x}) = -4\pi G \sum_{l=0}^{l_{max}} (A_l r^{-(l+1)} + B_l r^l) P_l(\nu), \quad (\text{A7})$$

with

$$A_l = \int_0^r \left[ \int_0^1 \rho(s, \nu) P_l(\nu) d\nu \right] s^l s^2 ds, \quad (\text{A8})$$

$$B_l = \int_r^\infty \left[ \int_0^1 \rho(s, \nu) P_l(\nu) d\nu \right] s^{-(l+1)} s^2 ds, \quad (\text{A9})$$

and where  $\nu = \sin \eta$ . The gravitational acceleration on the orbit is determined by differentiating equation A7 with respect to  $r$  and  $\eta$ .

We tested our expansion in a Kuzmin-Kutusov model (Dejonghe & de Zeeuw 1988) with  $a/c = 0.5$ , which corresponds to a very flat galaxy (about E5). This model has analytic density, potential, and accelerations. Truncating the expansion at  $P_6$  accurately reproduces the exact accelerations to 1% or better everywhere in the galaxy, so we set  $l_{max} = 6$  in equation (A7).

The additional acceleration from a mass point is straightforward to add to the radial component of the accelerations above. We store and model the galaxy in the angular range  $0^\circ \leq \eta \leq 90^\circ$ . We store the three lowest-order internal moments in each bin for each orbit (mass  $m$ ,  $m\mathbf{v}$ ,  $m\mathbf{v}\mathbf{v}$ ) for later use.

Simultaneously, the projected line-of-sight velocities are binned in a three-dimensional grid in projected radius  $R$ , angle  $\beta$  (measured from the major axis of the galaxy on the plane perpendicular to the line of sight), and velocity  $v$ . The spacing in  $R$  and  $\beta$  is defined as above. Since the orbits are being followed in  $r$  and  $\eta$ ,  $\phi$  is not defined. At each timestep, in order to project the orbit onto the line of sight, we choose 100 values of  $\phi$ , evenly spaced from 0 to  $\pi$ .

## A.2. Matching the Light Distribution and Observed Dynamics

The next step is to find the superposition of orbits consistent with the stellar mass distribution that best matches the observed LOSVDs. Richstone & Tremaine (1988) provide

an efficient method to match the mass distribution that can be augmented to minimize  $\chi^2$ . Their method maximizes an objective function

$$F = - \sum_i C_i(x_i) \quad (\text{A10})$$

while satisfying a set of constraints

$$Y_j = \sum_i m_{ij} x_i. \quad (\text{A11})$$

We choose to maximize the objective function

$$S - \alpha \chi^2 = - \sum_{i=1}^{N_{orb}} w_i \log \left( \frac{w_i}{\Delta \Omega_i} \right) - \alpha \sum_{k=1}^{N_d} \frac{(l_k - l_{k,o})^2}{\sigma_k^2}, \quad (\text{A12})$$

where  $w_i$  is the weight of the  $i^{th}$  orbit and  $l_k$  is the light in the  $k^{th}$  bin in the *observational* phase space composed of the position on the sky and the line of sight velocity. The more familiar LOSVD is the distribution of light in line of sight velocity at a single position on the sky. Thus the index  $k$  identifies a small range in both projected velocity and projected position. The variable  $\alpha$  is an adjustable parameter discussed further below. There are  $N_{orb}$  orbits in the orbit library, and  $k$  varies from 1 to  $N_d$ , where  $N_d$  is the number of positions at which the LOSVD has been measured times the number of velocity intervals at each measurement. The first sum in equation (A12) is an entropy, and the second is a  $\chi^2$  that measures the goodness of fit of the model LOSVDs to the observed LOSVDs. The sum of the orbits must also match the deprojected (3D) light distribution in the  $N_{bin}$  bins:

$$M_j = \sum_{i=1}^{N_{orb}} m_{ij} w_i \text{ for } j = 1, N_{bin}, \quad (\text{A13})$$

where  $m_{ij}$  is the mass contribution of the  $i^{th}$  orbit to the  $j^{th}$  bin.

In order to put equation (A12) in the form of equations (A10) and (A11), we make the following substitutions and identifications. First, we define  $x_i = w_i$  for  $i = 1, N_{orb}$ , and add an additional set of variables that measure the error in the light projected into each LOSVD bin  $x_{N_{orb}+k} = l_k - l_{k,o}$  for  $k = 1, N_d$ . Since the light in each bin of the model LOSVDs is given by the contribution of each orbit to that *projected* velocity and position there is an additional set of constraint equations of the form

$$l_{k,o} = \sum_{i=1}^{N_{orb}} m_{ij} w_i - x_j \text{ for } j = N_{bin} + 1, N_{bin} + N_d, \quad (\text{A14})$$

where  $k = j - N_{orb}$  and  $m_{ij}$  is the contribution of the  $i^{th}$  orbit to the  $k^{th}$  component of the set of LOSVDs.

Then we have

$$\begin{aligned} C_i &= x_i \log(x_i / \Delta \Omega_i) \quad \text{for } i \leq N_{orb} \\ C_i &= \alpha x_i^2 / \sigma_{i-N_{orb}}^2 \quad \text{for } N_{orb} < i \leq N_{orb} + N_d \end{aligned} \quad (\text{A15})$$

corresponding to equation (A10) and equations (A13) and (A15) correspond to equation (A11). Note that for  $i > N_{orb}$ ,  $-C_i$  is maximized at  $x_i = 0$ . The first set of  $C_i$  (for  $i \leq N_{orb}$ ) effectively keep the orbit weights positive. The second set (for  $i > N_{orb}$ ) minimizes the components of  $\chi^2$ . We then use the method described by Richstone & Tremaine (1988) to iteratively solve the equations.

An important feature of this problem is the choice of the parameter  $\alpha$ . Although we have not devised a method to specify appropriate values of this parameter in advance, if the quantity  $\chi^2$  reflects a satisfactory accounting of the estimates of errors in the recovery of the LOSVDs of the target galaxy, then the choice of  $\alpha$  and interpretation of the results is reasonably straightforward. A small  $\alpha$  will generally produce a solution. Increasing  $\alpha$  slowly decreases  $\chi^2$  but not beyond some limit. In practice, we start with  $\alpha = 0$  and increase it slowly until the change in  $\chi^2$  is less than 0.02 in a single iteration.

### A.3. A Test with a Black Hole

In this case we specify a dynamical model with a gravitational potential and a distribution function (DF) for the stars (the starlight need not, and does not, determine the mass in this model). The gravitational potential is

$$\Phi(r) = v_{\text{circ}}^2 \log(r) - \frac{GM_{\bullet}}{r}. \quad (\text{A16})$$

This potential includes a point mass and a flat circular-velocity curve (with velocity  $v_{\text{circ}}$ ) at large  $r$ . We investigated Michie-like DFs of the form

$$f = A \exp \left\{ - \left[ \frac{E + J_z^2 / (2\varpi_a^2)}{\sigma^2} \right] \right\} J_z^{2N} \sqcap (E_1, E, E_2), \quad (\text{A17})$$

where  $A$  is normalization,  $E$  and  $J_z$  are energy and angular momentum,  $w\varpi_a$  (an anisotropy distance),  $N$ , and  $\sigma$  (a velocity dispersion-like quantity) are model parameters, and  $E_1$  and  $E_2$  are upper and lower limits on the energy. The function  $\sqcap$  is defined by

$$\sqcap(E_1, E, E_2) = \begin{cases} 1 & \text{if } E_1 \leq E \leq E_2 \\ 0 & \text{otherwise.} \end{cases} \quad (\text{A18})$$

The DF can be rewritten as

$$f = \pi A \varpi^{2N} \exp(-\Phi/\sigma^2) \Pi(v_1, v_\phi, v_2) v_\phi^{2N} \exp(-v_\phi^2/(2\tilde{\sigma}^2)) \exp(-t^2/(2\sigma^2)) dt^2 dv_\phi, \quad (\text{A19})$$

where  $t^2 = v_\varpi^2 + v_z^2$ ,  $\tilde{\sigma}^2 = \sigma^2(\varpi_a^2/(\varpi_a^2 + \varpi^2))$  and  $v_i = \sqrt{2(E_i - \Phi)}$ . This function has a number of interesting properties:  $N > 0$  tends to create  $v_\phi$  enhanced anisotropy and a flattened density distribution;  $\tilde{\varpi}_a < \infty$  tends to depress  $v_\phi$  and create a prolate density distribution. The cutoffs in energy avert a divergence in the luminous matter distribution near the black hole.

The density is

$$\rho = 2\pi\sigma^2 A \varpi^{2N} \exp(-\Phi/\sigma^2) \int_{v_1}^{v_2} v_\phi^{2N} \exp(-v_\phi^2/(2\tilde{\sigma}^2)) [\exp(-t_1^2/(2\sigma^2)) - \exp(-t_2^2/(2\sigma^2))] dv_\phi, \quad (\text{A20})$$

where  $t_2 = v_2^2 - v_\phi^2$  and  $t_1 = \max(v_1^2 - v_\phi^2, 0)$ .

Note that the distribution functions with different choices of parameters can be added to each other (in the same potential) and similarly the densities and density-weighted moments are additive. A Monte Carlo realization of the model is constructed by sampling each density distribution and choosing the velocities randomly from the velocity distribution. Note that we have the additional freedom of choosing an arbitrary fraction of the  $\phi$  velocities in the positive sense, and hence setting the spin of any model between a maximum amount and zero. The total number of random variates chosen sets the normalization.

For the test here, we adopted a potential with  $v_{\text{circ}} = 220 \text{ km s}^{-1}$  and  $M_\bullet = 1.126 \times 10^8 M_\odot$ . We added two DFs. The first had  $\sigma = 160 \text{ km s}^{-1}$ ,  $\varpi_a = 600 \text{ pc}$ ,  $N = 0$ ,  $E_1 = \Phi(10 \text{ pc})$ ,  $E_2 = \Phi(1000 \text{ pc})$ , with equal numbers of the  $\phi$  velocities chosen in the positive and negative sense. The second DF had  $\sigma = 120 \text{ km s}^{-1}$ ,  $w_a = 200 \text{ pc}$ ,  $N = 2$ ,  $E_1 = 10 \text{ pc}$ ,  $E_2 = 1000 \text{ pc}$  and 3/4 of the  $\phi$  velocities were chosen positive. Each DF was assigned  $1/2 \times 10^9$  random points, so they had equal mass. The second DF, featuring a moderately spinning disk structure, dominates the model near the center of the galaxy, but declines rapidly. The first DF, a mildly prolate structure with no net spin dominates further out. No stars are found beyond a radius of 1000 pc from the center of the model. The  $10^9$  random points each are converted to projected positions and velocities (we assumed the galaxy was edge on), and binned into “observations” mimicing our combined HST and ground-based data, and also producing data mimicing data that would be obtained with an integral field unit. For the example below we used the IFU data with a resolution of 10 pc at the center, and lower resolution data extending to a distance of 800 pc from the center. At each location the projected velocity variates were binned at a resolution of  $20 \text{ km s}^{-1}$ . Gaussian noise was added to the data, in a series of 20 realizations. These datasets were then fed into the modeling program, which produced (in each case) a  $\chi^2$  map in  $v_{\text{circ}}$  and  $M_\bullet$ .

Marginalizing over each variable in turn produced the determinations of  $M_{\bullet}$  and  $v_{\text{circ}}$  illustrated in Figure 17. Each dataset had LOSVDs at 32 positions with 15 velocity bins, a product of 480. For each realization of this set, the best-fit model had a  $\chi^2$  near 500. Since the velocity bins are uncorrelated in these datasets this is about the expected  $\chi^2$ . For the presentation in Figure 17 the plots of  $\chi^2$  against black hole mass and  $v_{\text{circ}}$  were arbitrarily shifted to a minimum of 500. The error bars judged from the individual  $\chi^2$  profiles are about 20% smaller than the error (above) determined from the spread in minima. The mean values of  $M_{\bullet}$  and  $v_{\text{circ}}$  from these experiments were  $(1.15 \pm 0.03) \times 10^8 M_{\odot}$  and  $222 \pm 5 \text{ km s}^{-1}$ , in excellent agreement with the target values.

An earlier version of the code suffered from a units conversion error that led to an underestimate of black hole masses (and  $M/L$ ). All black hole masses obtained with this program published in or prior to 2003 should be multiplied by 1.09.

## REFERENCES

- Binney, J., Gerhard, O. E., & Hut, P. 1985, MNRAS, 215, 59
- Blandford, R. D., & McKee, C. F. 1982, ApJ, 255, 419
- Bower, G. A., et al. 2001, ApJ, 550, 75
- Cappellari, M., et al. 2002, ApJ, 578, 787
- Cecil, G., Greenhill, L. J., DePree, C. G., Nagar, N., Wilson, A. S., Dopita, M. A., Pérez-Fournon, I., Argon, A. L., & Moran, J. M. 2000, ApJ, 536, 675
- Chakrabarty, D., & Saha, P. 2001, ApJ, 122, 232
- Chary, R., et al. 2000, ApJ, 531, 756
- Contopoulos, G. 1956, Zeitschrift für Astrophysik, 39, 126
- Cretton, N., de Zeeuw, P. T., van der Marel, R. P., & Rix, H.-W. 1999, ApJS, 124, 383
- Dejonghe, H., & de Zeeuw, P. T. 1988, ApJ, 333, 90
- Fish, R. A. 1961, ApJ, 134, 880
- Gebhardt, K., et al. 1996, AJ, 112, 105
- Gebhardt, K., et al. 2000a, AJ, 119, 1157

- Gebhardt, K., et al. 2000b, *ApJ*, 538, 5
- Gebhardt, K., et al. 2003, *ApJ*, 583, 92
- Gerhard, O. E. 1993, *MNRAS*, 265, 213
- Ghez, A. M., et al. 2005, *ApJ*, 620, 744
- Herrnstein, J. R., et al. 1999, *Nature*, 400, 539
- Herrnstein, J. R., et al. 2005, *ApJ*, 629, 719
- Ho, L. C. 1999, *ApJ*, 516, 672
- Ho, L. C. 2008, *ARA&A*, 46, 475
- Ho, L. C., Flippenko, A. V., & Sargent, W. L. W. 1997, *ApJS*, 112, 315
- Jarrett, T. H., Chester, T., Cutri, R., Schneider, S., & Huchra, J. 2003, *AJ*, 125, 525
- Kormendy, J. 1982, in *Morphology and Dynamics of Galaxies*, ed. L. Martinet & M. Mayor (Sauverny: Geneva Observatory), p. 113
- Kormendy, J. 1983, *ApJ*, 275, 529
- Kormendy, J. 1984, *ApJ*, 286, 132
- Kormendy, J., & Richstone, D. 1992, *ApJ*, 393, 559
- Kormendy, J., & Richstone, D. 1995, *ARA&A*, 33, 581
- Lauer, T. R., Stover, R. J., & Terndrup, D. M. 1983, *The VISTA User’s Guide* (Lick Observatory Tech. Rept. No. 34).
- Lauer, T. R. 1985, *ApJS*, 57, 473
- Lauer, T. R. 1986, *ApJ*, 311, 34
- Lauer, T. R. 1999a, *PASP*, 111, 227
- Lauer, T. R. 1999b, *PASP*, 111, 1434
- Leitherer, C., et al. 2001, *STIS Instrument Handbook*, Version 5.1 (Baltimore: STScI)
- Lucy, L. B., 1974, *AJ*, 79, 745
- Magorrian, J., & Binney, J. 1994, *MNRAS*, 271, 949

- Marconi, A., et al. 2006, *A&A*, 448, 921
- Miyoshi, M., et al. 1995, *Nature*, 373, 127
- Netzer, H., & Peterson, B. M. 1997, in *Astronomical Time Series*, ed. D. Maoz, A. Sternberg & E. M. Leibowitz (Dordrecht: Kluwer), p. 85
- Pastorini, G. 2007, *A&A*, 469, 405
- Peterson, B. M. 1993, *PASP*, 105, 247
- Pinkney, J., et al. 2003, *ApJ*, 2003, *ApJ*, 596, 903
- Richardson, W. H. 1972, *J. Opt. Soc. A.*, 62, 52
- Richstone, D. O., & Tremaine, S. D. 1988, *ApJ*, 327, 82
- Sandage, A., Freeman, K. C., & Stokes, N. R. 1970, *ApJ*, 160, 831
- Schwarzschild, M. 1979, *ApJ*, 232, 236
- Seigar, M., Carollo, C. M., Stiavelli, M., de Zeeuw, P. T., & Dejonghe, H. 2002, *AJ*, 123, 184
- Silge, J. D., & Gebhardt, K. 2003, *AJ*, 125, 2809
- Silge, J. D., Gebhardt, K., Bergmann, M., Richstone, D. 2005, *AJ*, 130, 406
- Thomas, J., et al. 2004, *MNRAS*, 353, 391
- Thomas, J., et al. 2005, *MNRAS*, 360, 1355
- Tonry, J. L., et al. 2001, *ApJ*, 546, 681
- Tremaine, S., et al. 1994, *AJ*, 107, 634
- Valluri, M., Merritt, D., & Emsellem, E. 2004, *ApJ*, 602, 66
- van Albada, G. D. 1980, *A&A*, 90, 123
- van der Marel, R. P., Cretton, N., de Zeeuw, P., & Rix, H.-W. 1998, *ApJ*, 493, 613
- van der Marel, R. P., & Franx, M. 1993, *ApJ*, 407, 525
- Verdoes Kleijn, G. A., van der Marel, R. P., Carollo, C. M., & de Zeeuw, P. T. 2000, *AJ*, 120, 1221

Fig. 1.— Ground-based NIR images of NGC 4258 identifying large-scale morphological characteristics of the galaxy: The bulge ( $\text{PA} \simeq 146^\circ$ ), which is embedded in the inner oval disk ( $\text{PA} \simeq 156^\circ$ ); the weak bar ( $\text{PA} \simeq 11^\circ$ ); and the outer oval disk ( $\text{PA} \simeq 150^\circ$ ). *Top left*: 2MASS composite  $J+H+K$  image. Intensity is proportional to the square root of surface brightness to illustrate the bulge and the small bar. The scale is  $1'' \text{ pixel}^{-1}$  and the image size is  $17'.1 \times 17'.1$ . *Top right*: As before, but intensity is proportional to surface brightness; the inner oval disk is now saturated and the outer oval disk becomes more prominent. *Bottom left*:  $K$ -band image using SQUID on the KPNO 2.1-m telescope. Intensity is proportional to the square root of surface brightness to illustrate the bulge. The scale is  $0''.69 \text{ pixel}^{-1}$  and the image size is  $5'.9 \times 5'.9$ . *Bottom right*: As before, but intensity is proportional to surface brightness to illustrate the weak bar.

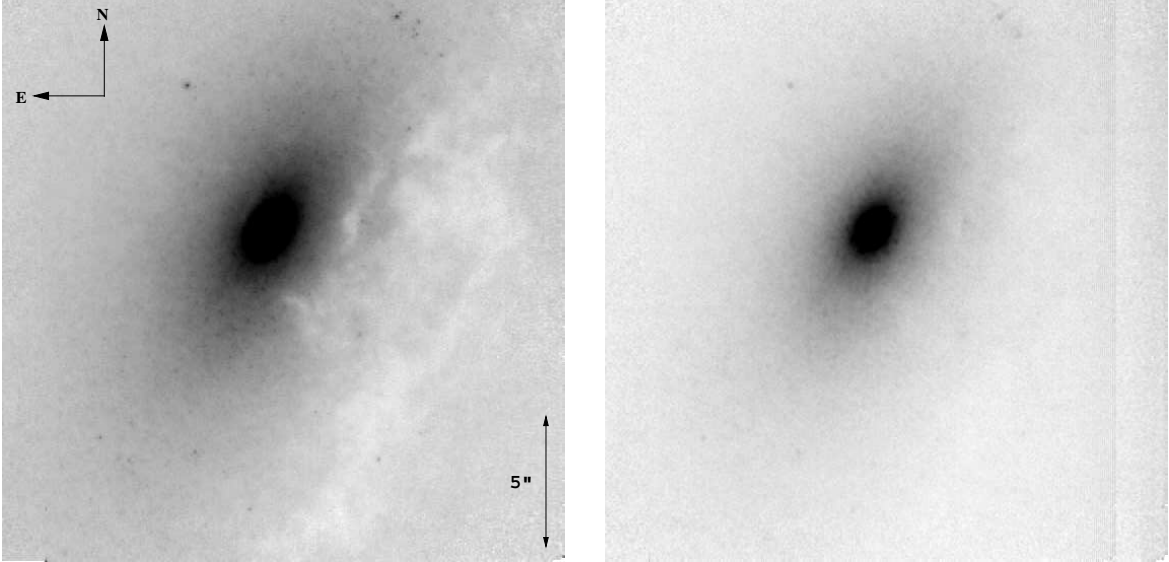


Fig. 2.— *HST* NICMOS images of NGC 4258 in the  $J$  band (F110W) (left) and in the  $K$  band (F222M) (right), from Chary et al. (2000). In both images, the scale and size are  $\sim 0''.038 \text{ pixel}^{-1}$  and  $\sim 21'' \times 21''$ , respectively. The images are not deconvolved. Intensity is proportional to the square root of surface brightness. A band of data is missing on the right side of the  $K$ -band image. For the extraction of stellar mass profiles from these images, the dust on the SW side was corrected by replacing the SW side of the galaxy with the NE side flipped across the major axis.



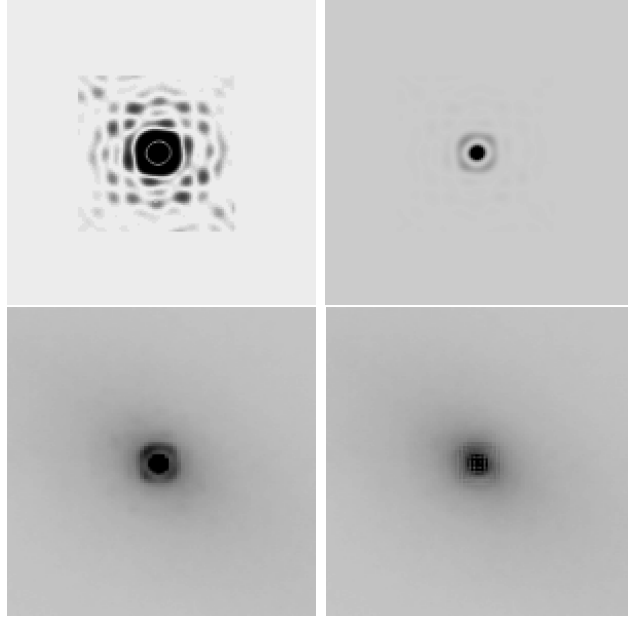


Fig. 3.— *HST* NICMOS *K*-band images of the central  $5''.7 \times 5''.7$  of NGC 4258, adapted from the images provided by Chary et al. (2000). North is up, and East is to the left. *Top left*: The TinyTim model PSF shown at a nonlinear stretch (higher contrast at lower surface brightnesses) to emphasize the small-scale features. *Top right*: Same as before, but now scaled to the galaxy image and at the same linear stretch as in bottom row. *Bottom left*: The galaxy before PSF subtraction; the AGN is evident. *Bottom right*: The adopted PSF-subtracted galaxy image that was used to provide the central brightness profile in the *K* band. In the end, the AGN could not be subtracted well enough in *K*, and the *J*-band profile was used for  $r < 0''.2$ .

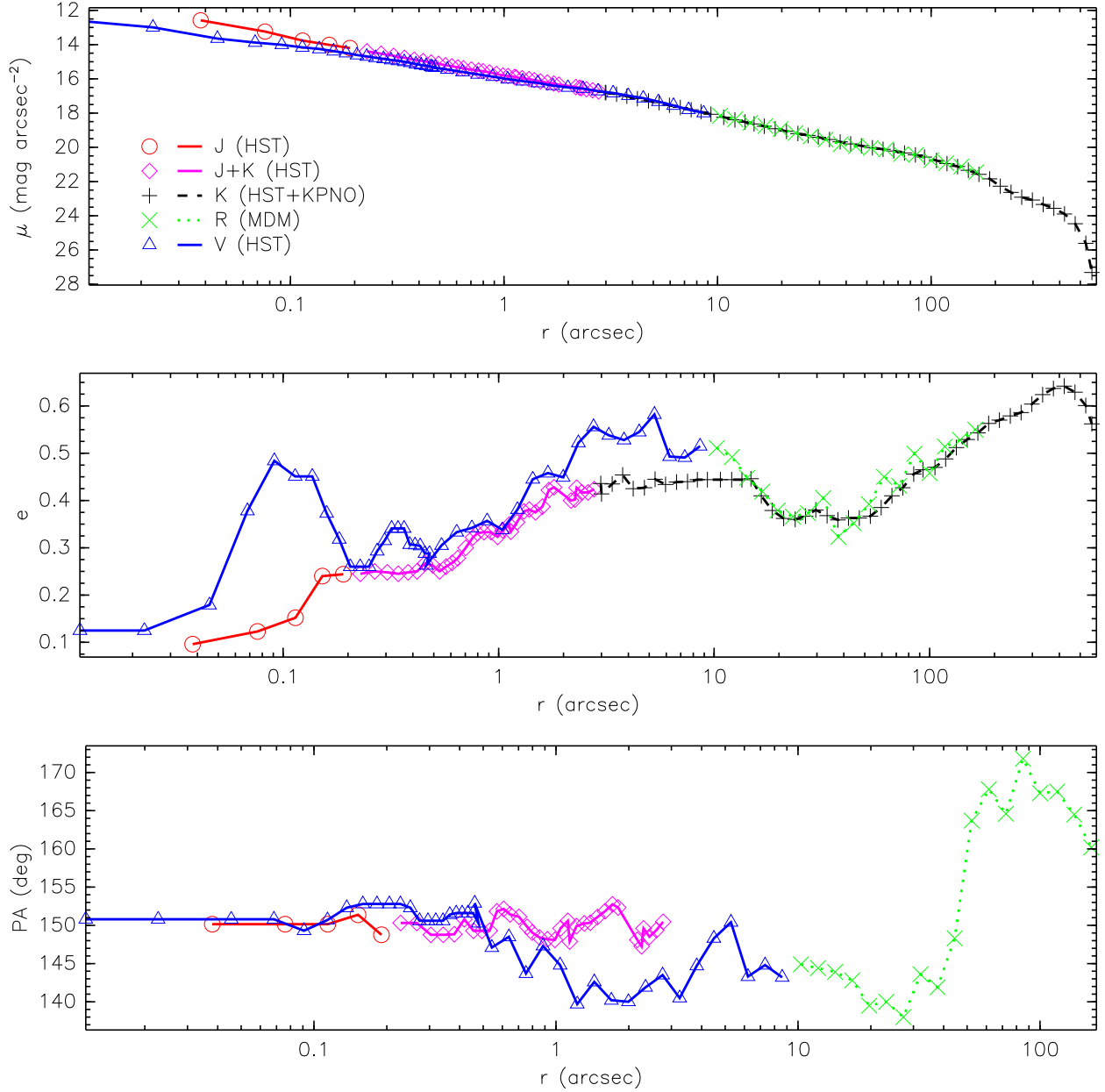


Fig. 4.— NGC 4258 major-axis surface photometry *after* subtraction of prominent dust lanes, and correction for the AGN. The radius ( $r$ ) is measured along the major axis. All *HST* profiles are deconvolved for  $r < 3''$ . *Top*: NIR ( $J$ ,  $J+K$ ,  $K$ ) and optical ( $V$ ,  $R$ ) surface brightness profiles. The  $R$ -band profile is calibrated using the *HST*  $V$ -band zeropoint between  $r \simeq 5''$  and  $7''$ . The NIR profiles are scaled to match the optical profile at large radii to illustrate the absence of major color gradients in the disk. The almost power-law profile at  $r \lesssim 40''$  belongs to the bulge. Only data out to  $r \approx 150''$  are used for the dynamical modeling. *Middle*: The ellipticity as a function of radius. *Bottom*: The position angle of the major axis as a function of radius.

Fig. 5.— Ground-based image of NGC 4258 in the  $R$  band taken with the MDM 1.3-m McGraw Hill telescope. The square is centered on the nucleus, and is  $8''$  on a side. The scale of the CCD was  $0''.508 \text{ pixel}^{-1}$ . A logarithmic stretch has been applied, and set to prevent “overexposure” of the bulge region.

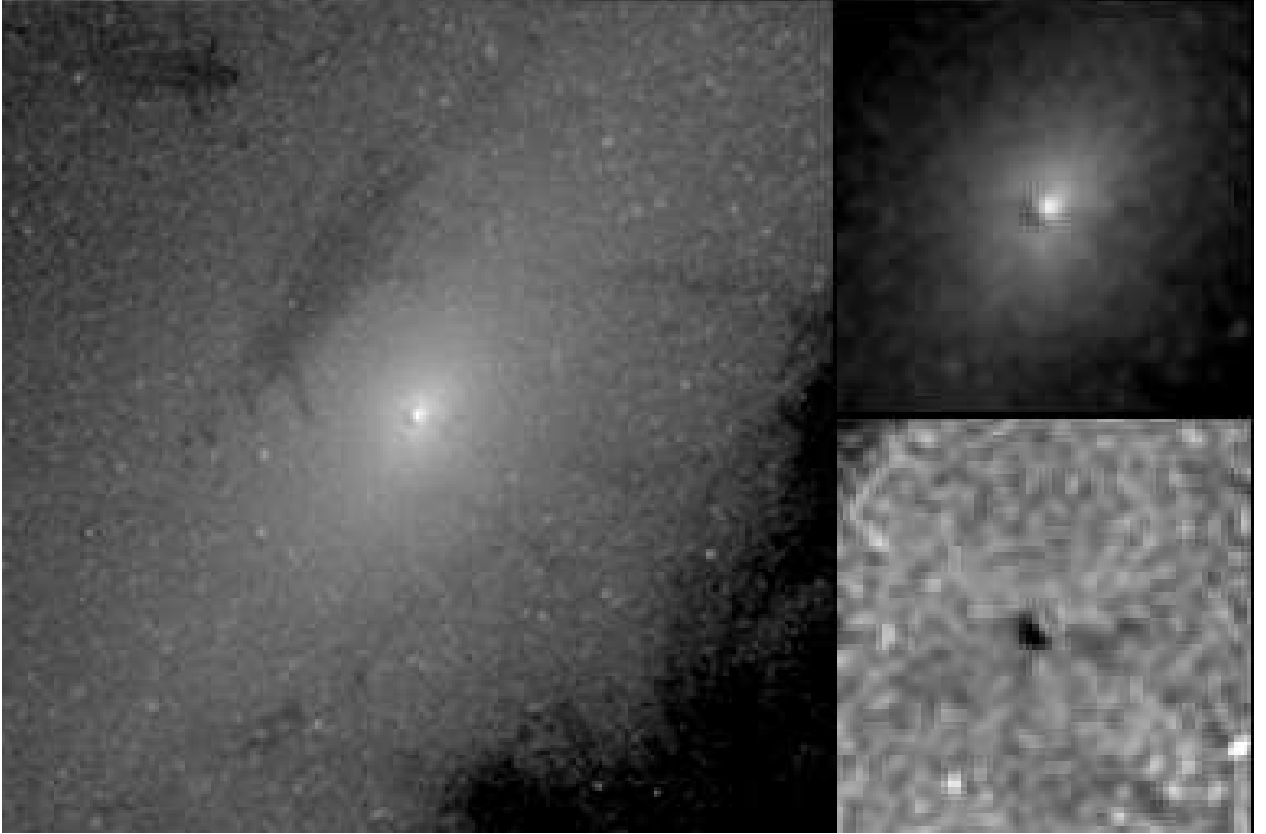


Fig. 6.— *HST* WFPC2 image of NGC 4258. The large panel shows the central  $256 \times 256$  pixels of the deconvolved F547M Nyquist-sampled image. It corresponds to  $128 \times 128 \text{ PC1}$  pixels, or  $5''.84 \times 5''.84$ . An arbitrary logarithmic stretch has been applied. The small upper-right panel is the central  $1''.48 \times 1''.48$  ( $64 \times 64$  subpixels) of the same image, magnified by a factor of 2 compared to the larger panel. Again a logarithmic stretch has been applied, but with greater contrast over the nuclear region. The bottom-right panel shows the same region divided by a model reconstructed from the surface photometry. North is up and East to the left.

Fig. 7.— Color map of the nuclear region of NGC 4258. It corresponds approximately to  $V - I$ , and was created from the ratio of the F547M image to the F791W image. Darker is redder. The map size is  $8''.0 \times 7''.2$ . The F791W image had each pixel resampled into 4 pixels to match the F547M image, and was then boxcar-smoothed. The central blue spike is not accurate because the center is saturated in the F791W data, and the F547M and F791W images are not perfectly aligned.

Fig. 8.— Color composite image of NGC 4258. Red corresponds to F791W, green to F656W, and blue to F300W. The image has a size of  $476 \times 526$  pixels, with a scale of  $0.0455'' \text{ pix}^{-1}$ . North is up, and East to the left.

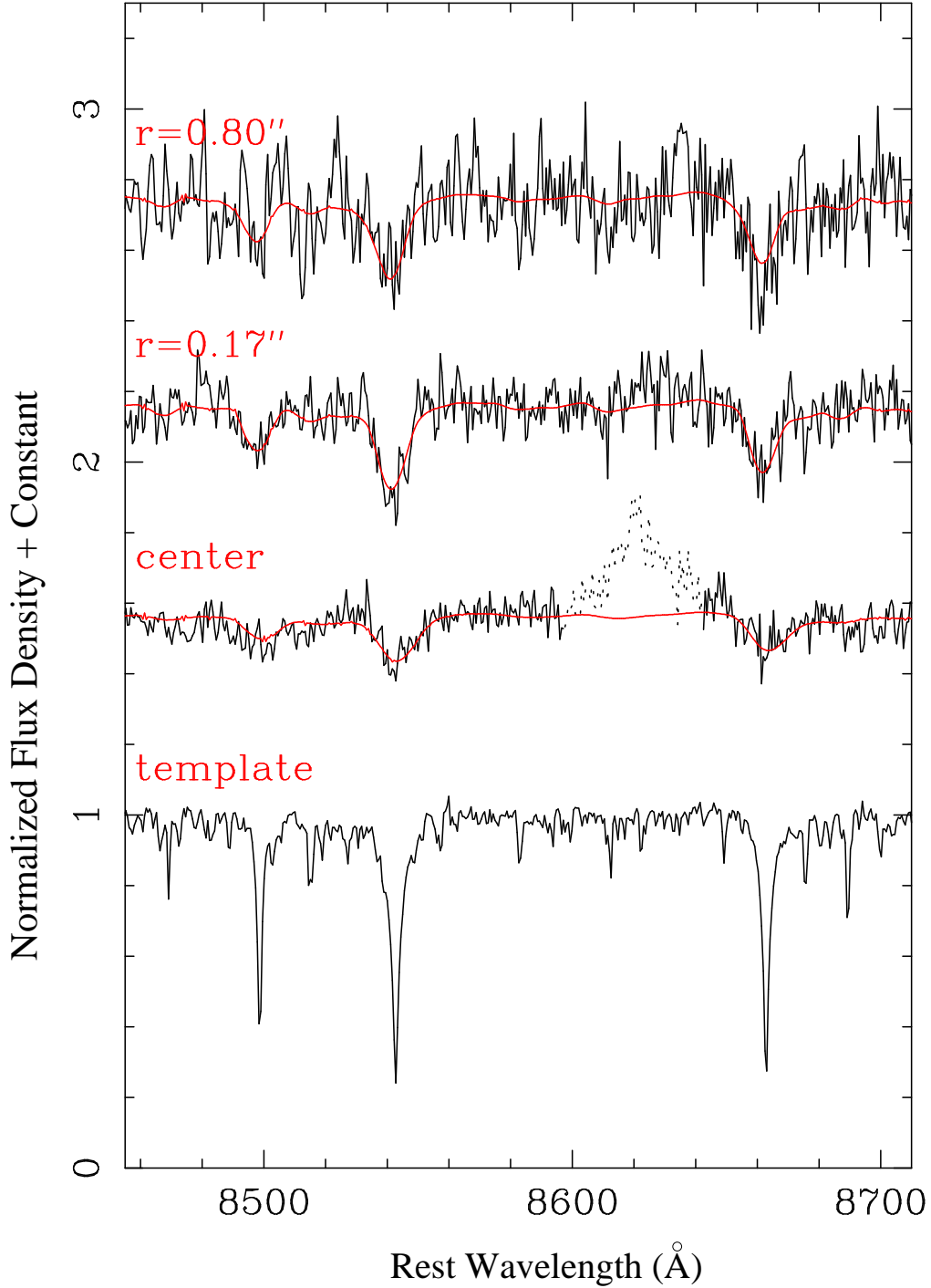


Fig. 9.— Sample STIS spectra extracted from the central and two outer spatial bins on the approaching (SE) side of the galaxy, as well as of the template star HR 7615 which was used for the LOSVD deconvolution. The smooth solid lines superimposed on the galaxy spectra are the template stellar spectra convolved with the derived LOSVDs. The emission-line feature (probably Fe II) in the nuclear spectrum (dotted) was subtracted before the LOSVD analysis was performed.

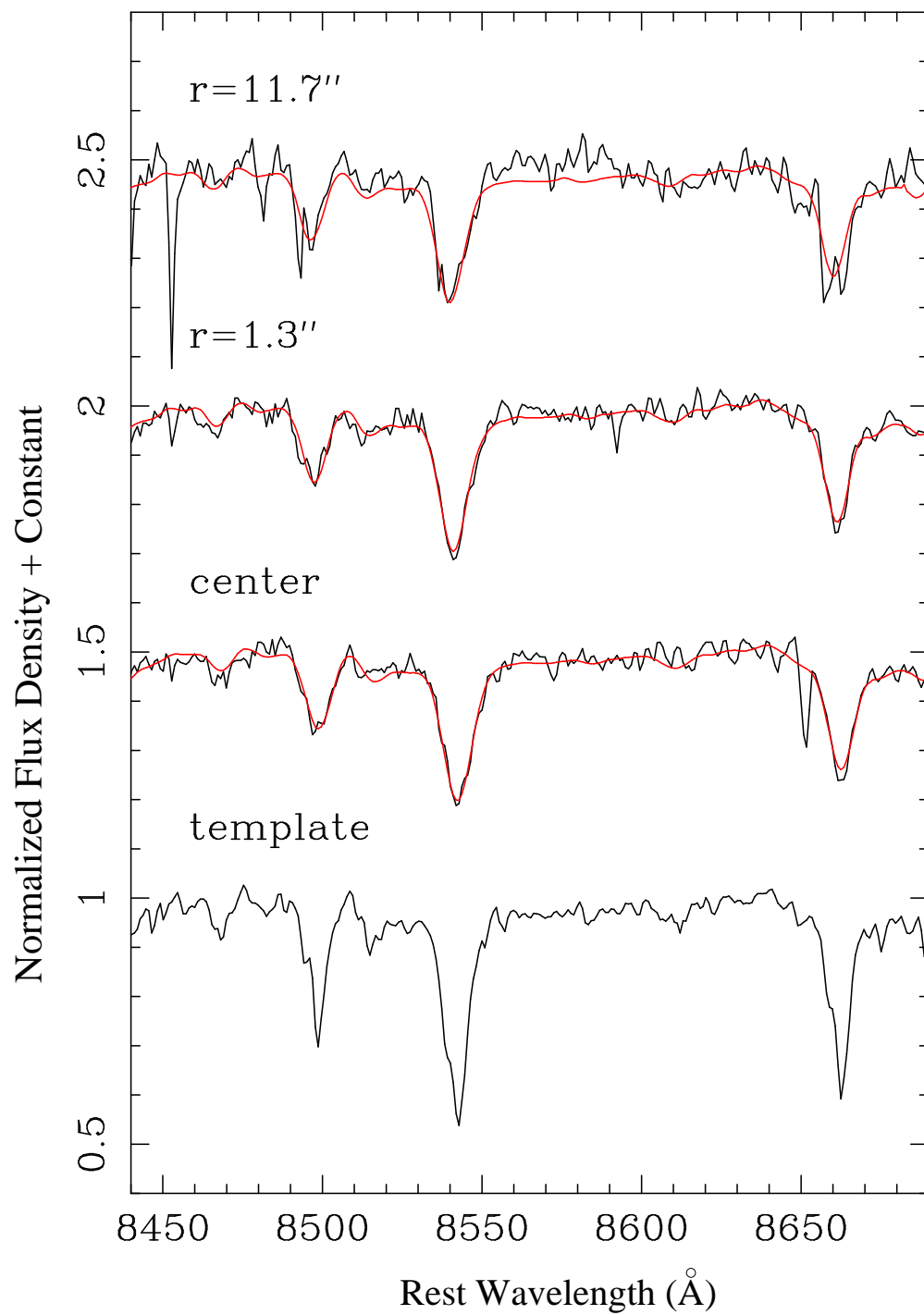


Fig. 10.— As Figure 9 but for the ground-based spectra obtained with Modspec at MDM.

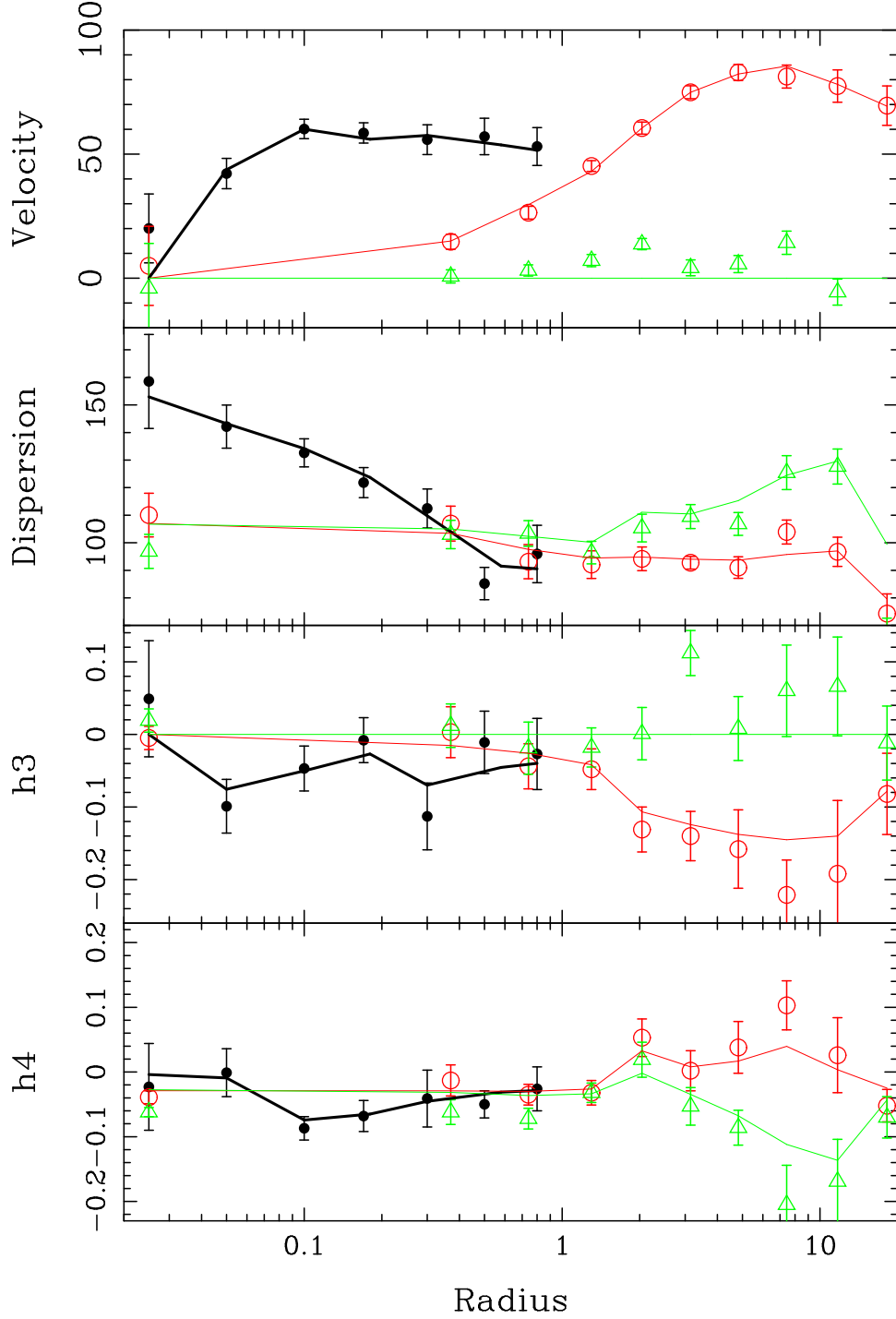


Fig. 11.— Gauss-Hermite moments of the symmetrized LOSVDs as a function of position for the data and one model. Black filled circles are from the STIS data on the major axis. Red open circles are ground-based major axis data. Green triangles are ground-based minor axis data. The solid lines represent the analogous quantities derived from the LOSVDs of the base model described in §5.1.

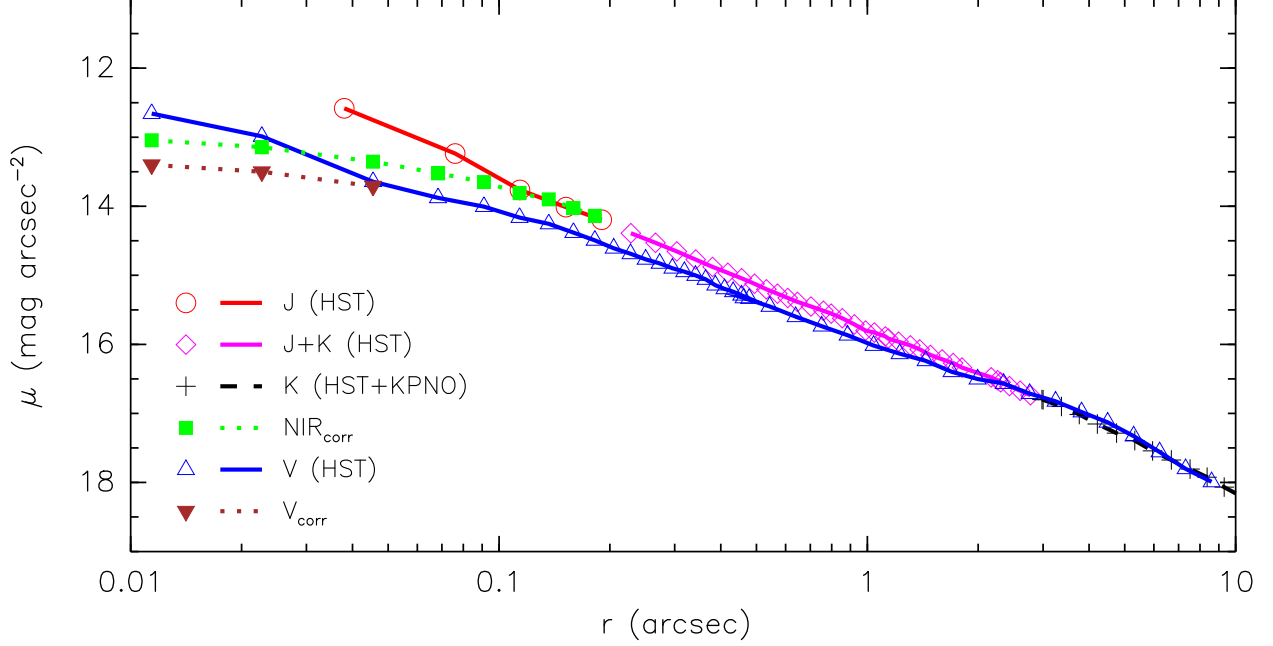


Fig. 12.— NGC 4258 major-axis surface photometry: the central  $10''$ . Photometric calibration is as in Figure 4. For  $r \lesssim 2''$  there is a color gradient between the  $V$  and the NIR ( $J$ ,  $J+K$ , and  $K$  spliced together) profiles. The  $V_{\text{corr}}$  profile is identical to  $V$  except the inner three points are replaced with an arbitrary “core” profile. The  $\text{NIR}_{\text{corr}}$  profile is created from NIR by replacing the points inward of  $r = 0''.2$  with points that follow the  $V_{\text{corr}}$  profile, shifted by an amount equal to the color difference between NIR and  $V_{\text{corr}}$  at  $r = 0''.2$ . All profiles extend to  $r > 10''$  as shown in Figure 4. In the  $\text{NIR}_{\text{corr}}$  and  $V_{\text{corr}}$  plots, only the points that differ from the NIR and  $V$  profiles, respectively, are shown.  $\text{NIR}_{\text{corr}}$  and  $V_{\text{corr}}$  are used to probe the effect of an unresolved AGN on the black hole mass, as discussed in §5.4; they are meant to represent limiting cases, *not* accurate corrections to the AGN contamination.



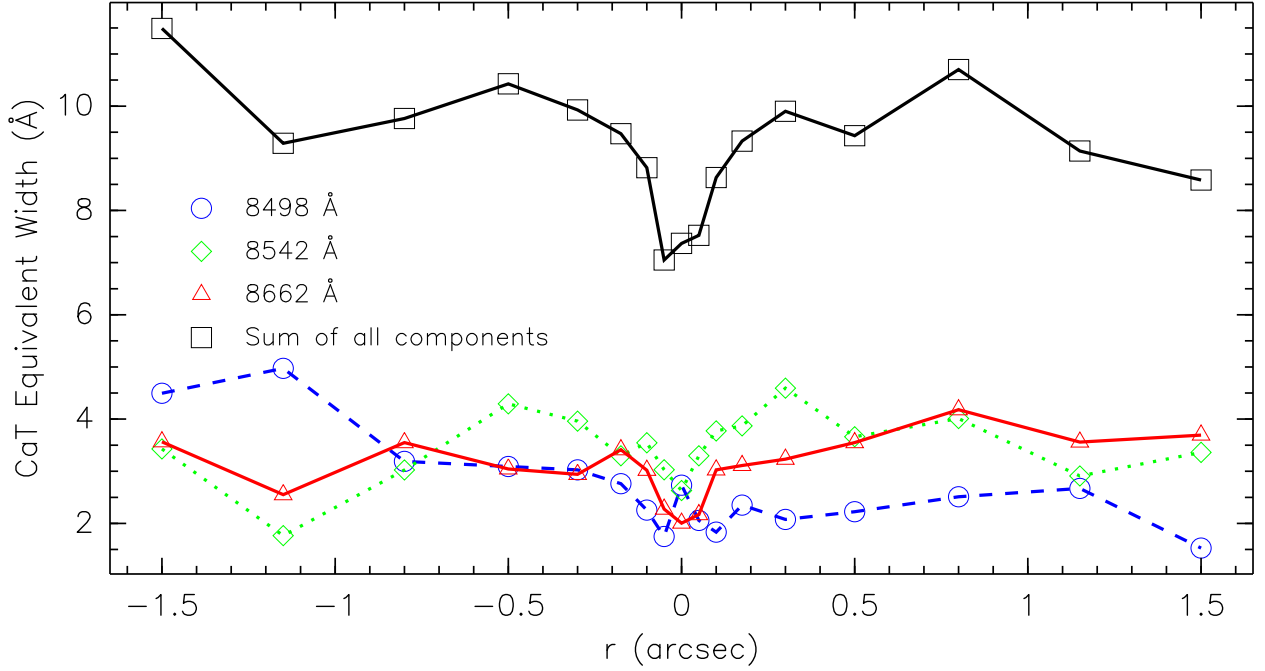


Fig. 13.— Equivalent width (EW) profiles along the major axis for each component of the Ca II triplet (CaT) line, and for the sum of their EWs. All data points are computed from the STIS spectrum. The subtraction of the emission line near the center (see Figure 9) may have affected the EW estimate for the 8662 Å component. The 8498 Å component, although furthest away from the emission line, has a low S/N and hence its EW profile may be less reliable. Furthermore, the S/N of the spectra drops rapidly with increasing radius. Nevertheless, the summed profile shows clearly that the spectrum within  $r < 0''.2$  is contaminated at the  $\sim 30\%$  level by some source of smooth, lineless continuum light, such as an AGN or OB stars. The positive- $r$  direction corresponds to the approaching (SE) side of the galaxy.

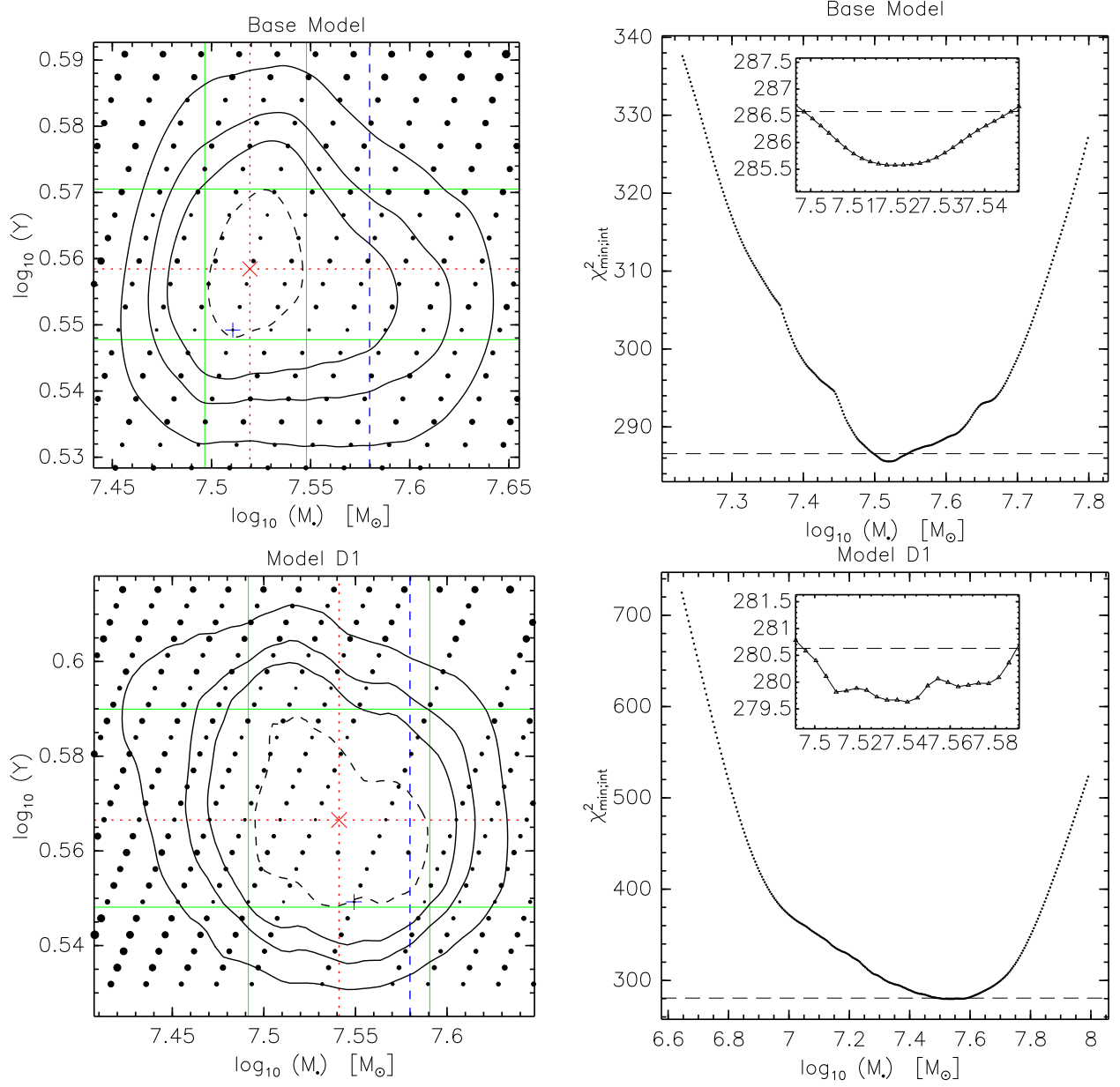


Fig. 14.— *Left:* Contour maps of  $\chi^2(M_\bullet, \Upsilon)$  for the dynamical models bearing the parameters listed in Table 4. Model names are as in Table 4. The stellar  $M/L$  ratio ( $\Upsilon$ ) refers to the  $V$  band. Each dot represents a model, and dot size is proportional to the value of  $\chi^2$  for that model. The symbol “+” corresponds to the “best” model ( $\chi^2_{\min}$ ). The symbol “X” corresponds to the minimum interpolated  $\chi^2$ . The contour levels are drawn for  $\Delta\chi^2 \equiv \chi^2 - \chi^2_{\min;\text{int}} = 1.0$  (dashed), 2.71, 4.0, and 6.63, corresponding to confidence levels of 68%, 90%, 95%, and 99%, respectively, for one degree of freedom. The horizontal and vertical solid lines indicate the nominal “ $1\sigma$ ” one-dimensional uncertainties. The vertical dashed line indicates the maser mass. *Right:* Values of  $\chi^2_{\min;\text{int}}$  marginalized over the  $\Upsilon$  axis. The horizontal dashed line indicates the  $\Delta\chi^2 = 1$  level.

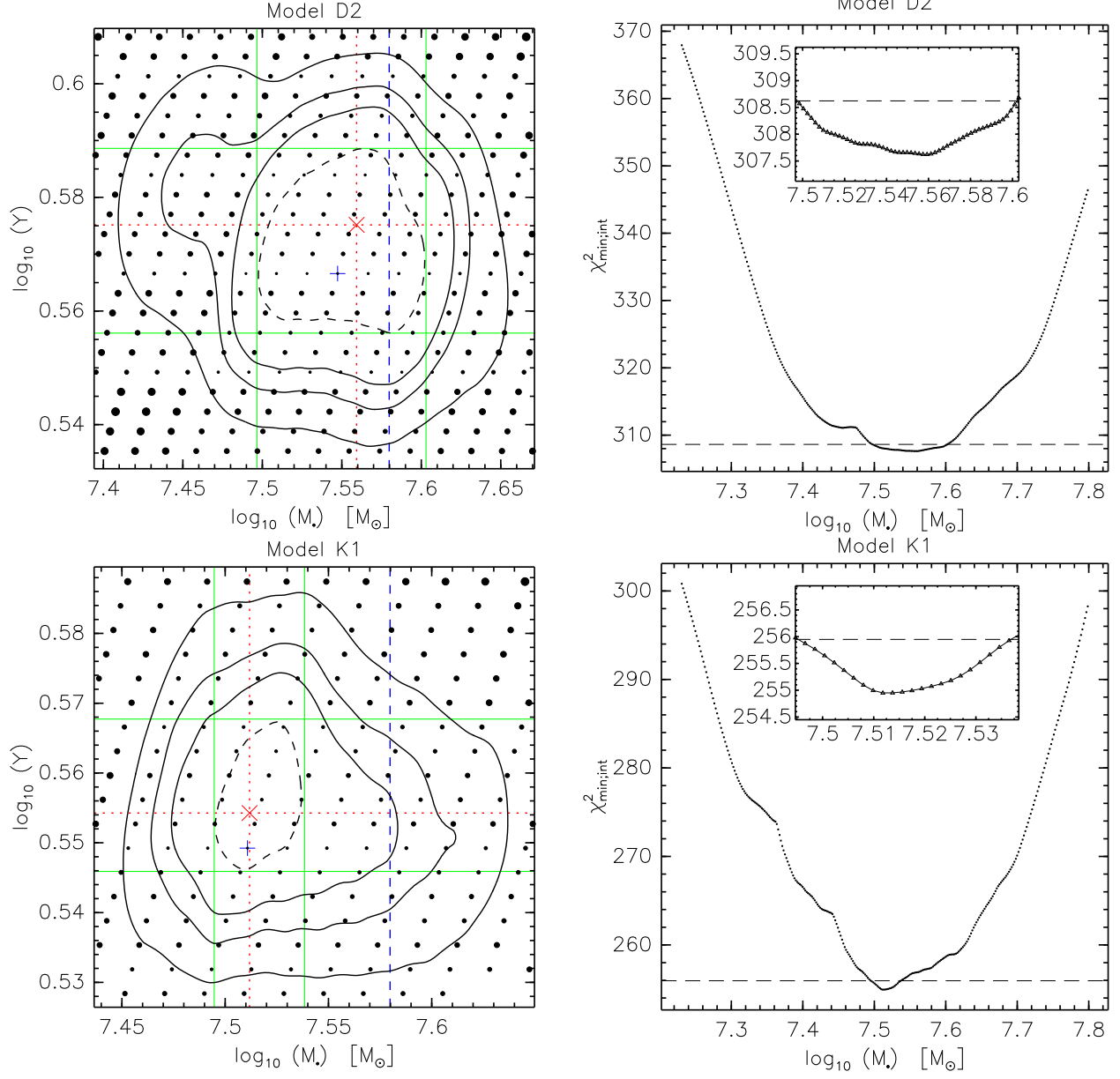


Fig. 14.— Continued

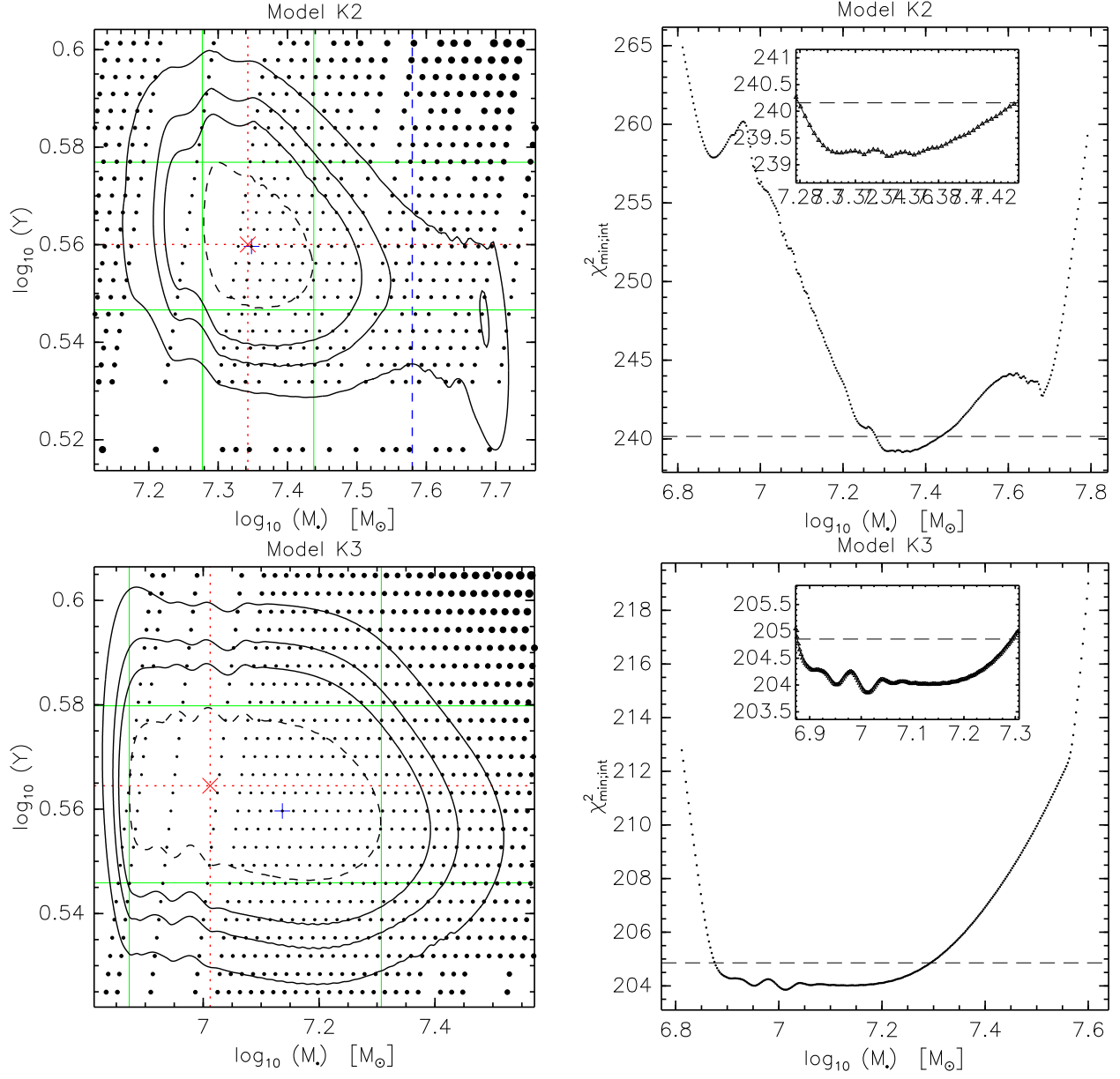


Fig. 14.— Continued

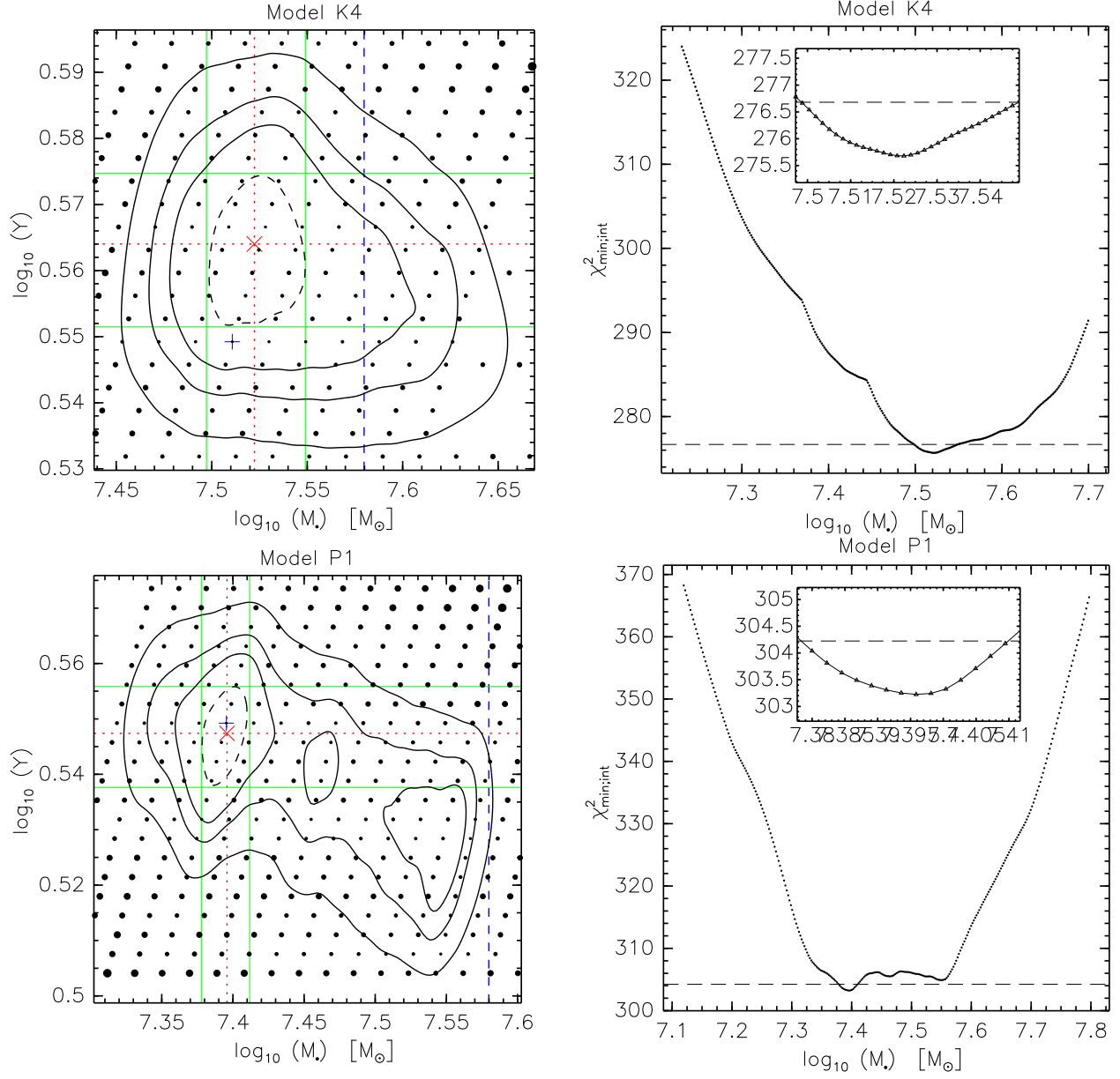


Fig. 14.— Continued

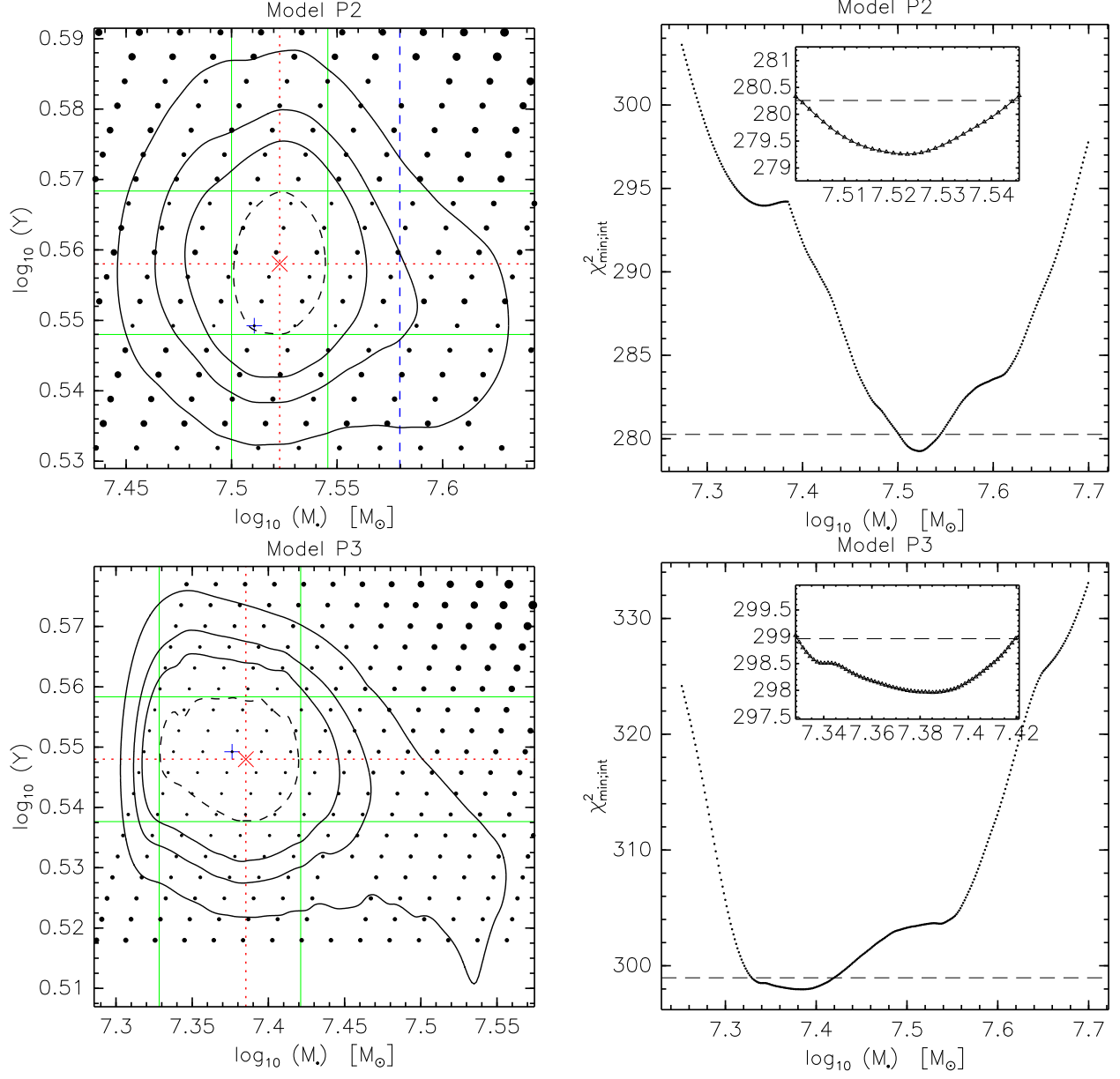


Fig. 14.— Continued

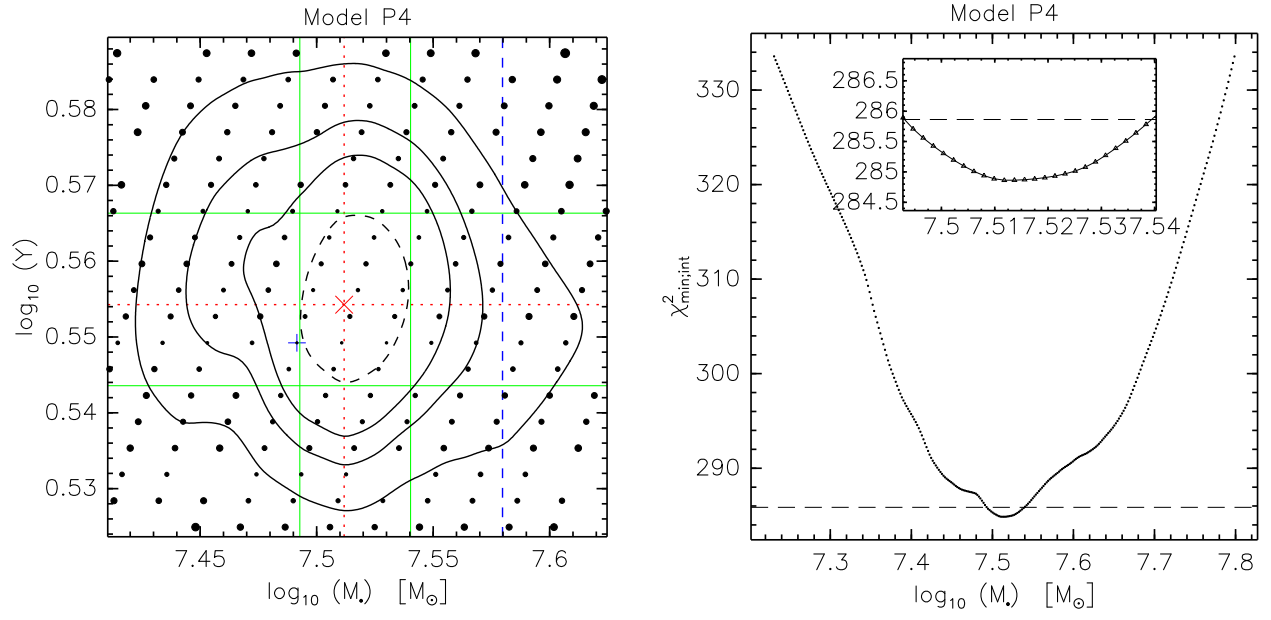


Fig. 14.— Continued

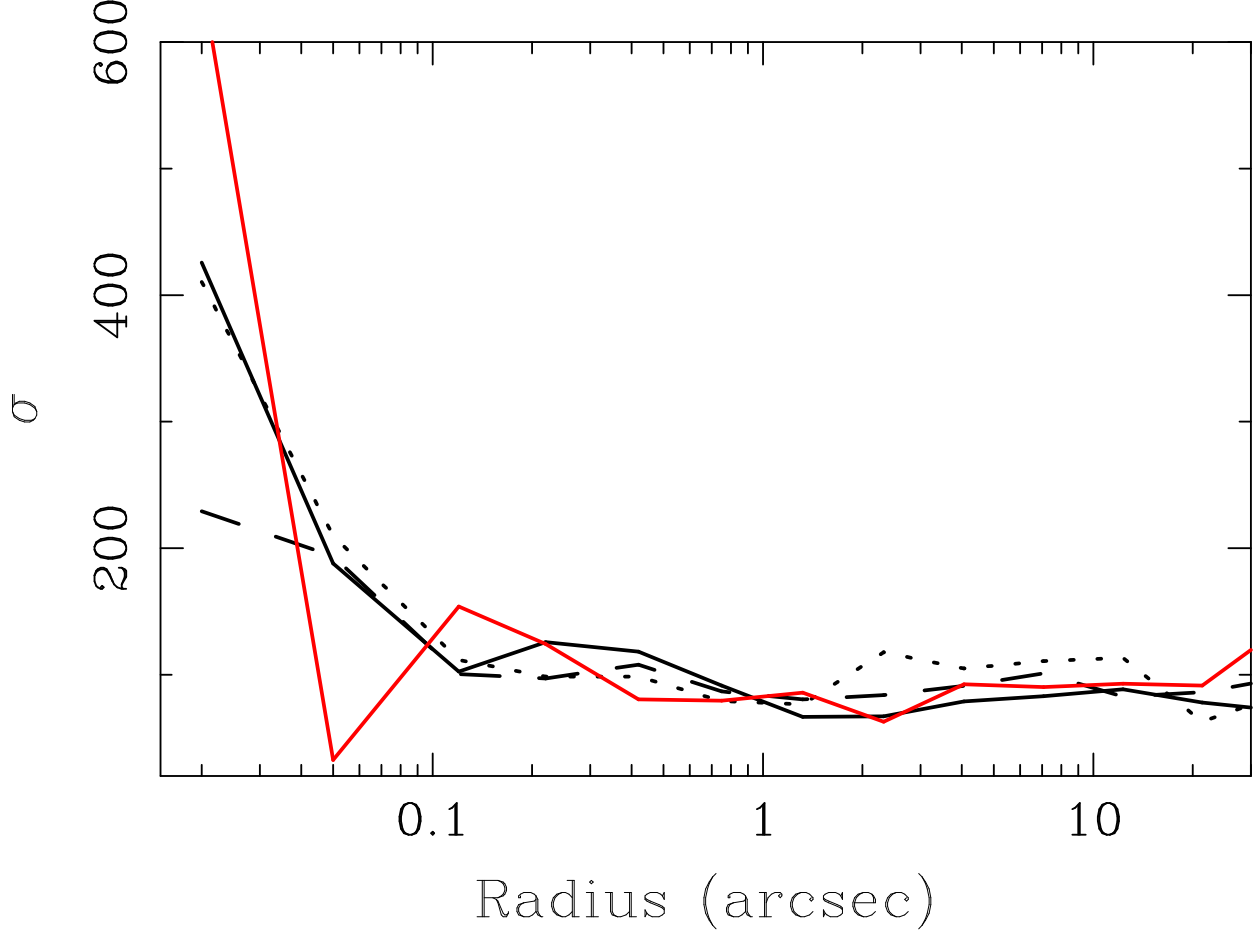


Fig. 15.— Internal moments of the baseline model in the equatorial plane. The red line illustrates the mean rotational velocity  $\langle v_\phi \rangle$  and the dotted line is the velocity dispersion in the  $\phi$  direction  $\sigma_\phi = \sqrt{\langle v_\phi^2 \rangle - \langle v_\phi \rangle^2}$ . The solid line is the radial dispersion  $\sigma_r$  and the dashed line is  $\sigma_\theta$ .



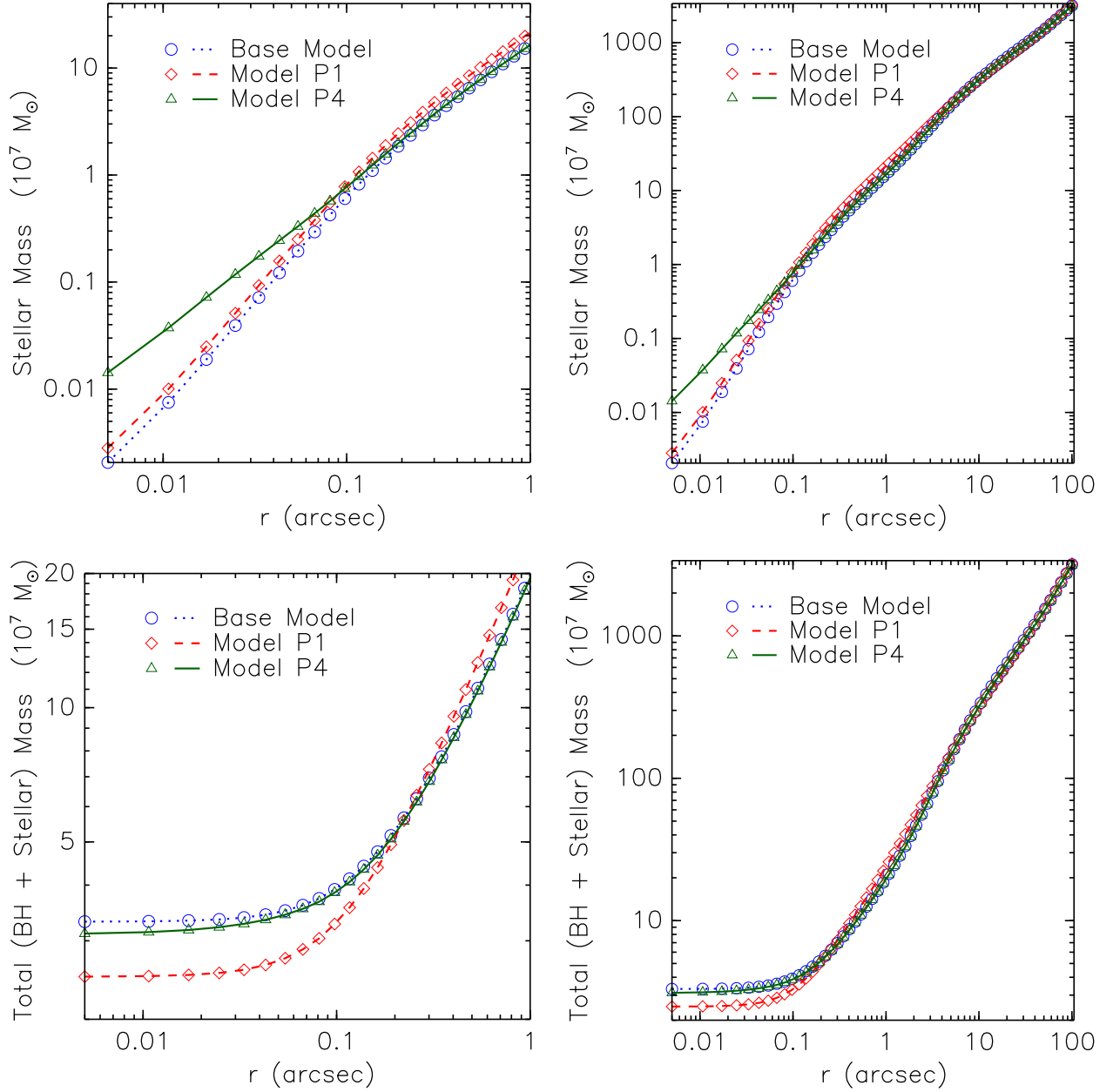


Fig. 16.— The enclosed stellar mass  $M_*$  (top row), and the sum of the black hole mass and the enclosed stellar mass  $M_\bullet + M_*$  (bottom row), as a function of model radius. The base model and model P4 are constrained by the same kinematic dataset, and they share the same mass  $V$ -band profile for  $r > 0''.04$  (see Table 4). Because of the degeneracy between  $M_\bullet$  and  $M_*$  within a small radius  $r_0 \approx 0''.1$  from the center, comparable to the spatial resolution of the kinematic data, the modeling algorithm can only constrain the total mass inside that radius. As a result, model P4 is assigned a slightly lower  $M_\bullet$  to compensate for the excess mass contained in the central “bump” of its mass profile. Model P1 is characterized by the  $\text{NIR}_{\text{corr}}$  mass profile, which differs from that of both P4 and the base model at  $r > r_0$ .

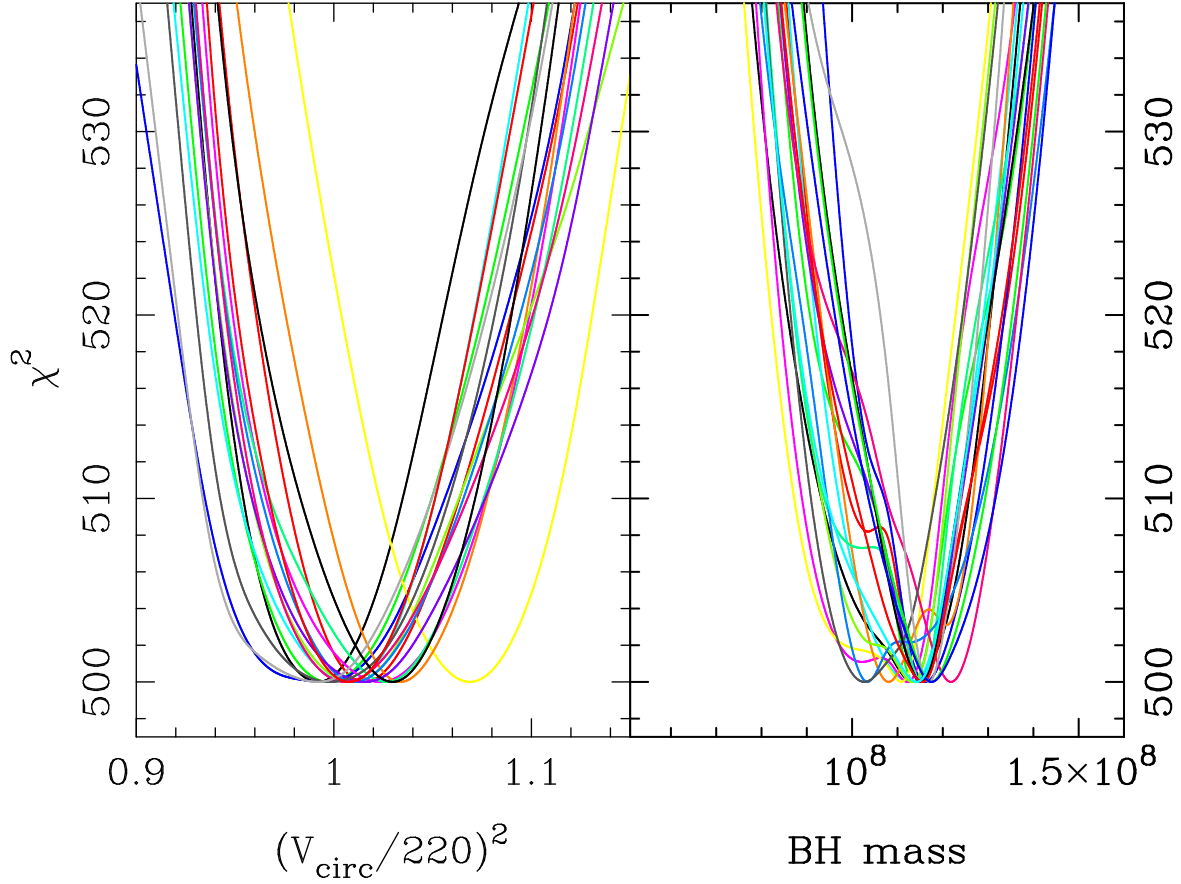


Fig. 17.—  $\chi^2$  profiles of orbit-based models of the Monte Carlo model described in the Appendix A.3. The left panel illustrates the recovery of the circular velocity of the potential for 20 different realizations of its LOSVDs. The right panel illustrates the recovery of the black hole mass from the same set of realizations. The plots in each panel are marginalized over the variable in the other panel. The mean of the derived black hole masses is  $1.15 \times 10^8 M_\odot$ , consistent with the model mass.

Table 1. JOURNAL OF IMAGING OBSERVATIONS OF NGC 4258

Instrument	Filter/Band	Radial Range	Source
<i>HST</i> NICMOS <sup>a</sup>	F110W, F160W, F222M <sup>b</sup>	$r < 9''$	Chary et al. (2000)
KPNO <sup>c</sup> 2.1-m	$K$	$2'' \leq r < 32''$	This paper
2MASS <sup>d</sup>	$J, H, K$	$r \geq 32''$	Jarrett et al. (2003)
<i>HST</i> WFPC2 <sup>e</sup>	F791W <sup>f</sup>	$r < 9''$	Cecil et al. (2000)
MDM 1.3-m	$R$	$r \geq 9''$	This paper
<i>HST</i> WFPC2	F547M <sup>g</sup>	$r < 9''$	This paper

<sup>a</sup>Near Infrared Camera and Multi-Object Spectrometer.

<sup>b</sup>Corresponding, approximately, to the  $J$ ,  $H$ , and  $K$  bandpasses, respectively.

<sup>c</sup>Kitt Peak National Observatory.

<sup>d</sup>Two Micron All Sky Survey.

<sup>e</sup>Wide Field and Planetary Camera 2.

<sup>f</sup>Corresponding, approximately, to the  $I$  bandpass.

<sup>g</sup>Corresponding, approximately, to the  $V$  bandpass.

Table 2. LONG-SLIT SPECTROGRAPH CONFIGURATIONS

Instrument <sup>a</sup> + grating	Slit size " × "	$\lambda_{\text{cen}}$ <sup>b</sup> Å	$\lambda$ -range <sup>b</sup> Å	Disp <sup>-1</sup> <sup>c</sup> Å pix <sup>-1</sup>	Comp. line $\sigma$ <sup>d</sup> Å (km s <sup>-1</sup> )	Scale <sup>e</sup> " pix <sup>-1</sup>
STIS + G750M	52×0.1	8561	8275–8847	0.554	0.45 (12.4)	0.051
Wilbur + 831g/mm	540×0.9	8500	8100–9020	0.90	0.9 (32)	0.37
Echelle + 831g/mm	540×0.9	8500	8100–9020	1.46	0.9 (32)	0.59

<sup>a</sup>Wilbur and Echelle are two of the CCDs used on the Modspec instrument at the MDM 2.4-m telescope.

<sup>b</sup>Central wavelength and wavelength range. STIS values taken from the STIS Instrument Handbook (Leitherer et al. 2001, pp. 231, 234). For Modspec, we show the range extracted.

<sup>c</sup>Reciprocal dispersion was measured using our own wavelength solutions. The distribution of dispersion solutions for a given dataset had a  $\sigma \approx 0.00015$  Å pix<sup>-1</sup>. The average dispersion given in the Handbook for G750M is 0.56 Å pix<sup>-1</sup>.

<sup>d</sup>Instrumental line widths measured by fitting Gaussians to emission lines on comparison lamp exposures. This gives an estimate of the instrumental line width for *extended* sources. We use  $\sim 5$  lines per exposure, and at least 5 measurements per line. All of the G750M observations used an unbinned 1024×1024 pixel CCD. Leitherer et al. (2001) (p. 300) give an instrumental line width for *point* sources of  $\sigma=13.3$  km s<sup>-1</sup> for the STIS + G750M configuration.

<sup>e</sup>The spatial scale along the slit is constant, but it varies across the slit from one grating to the next. It is 0".05597 pix<sup>-1</sup> for G750M at 8561 Å and 0".05465 pix<sup>-1</sup> for G750M at 6581 Å (STIS ISR 98-23).

Note. — Some numbers for the CCDs Wilbur and Echelle on Modspec are calculated by the program “modset” by J. Thorstensen. The slit width, spectral resolution, and spatial resolution varied for the Modspec observations; typical measured values are shown here.

Table 3. KINEMATIC PARAMETER PROFILES OF NGC 4258

$R$ (")	$V$	$\sigma$	$H3$	$H4$
<i>HST</i> STIS – Major axis profile (PA = 140°)				
0.00	20 ± 14	159 ± 17	0.05 ± 0.08	-0.02 ± 0.07
0.05	42 ± 6	142 ± 8	-0.10 ± 0.04	0.00 ± 0.04
0.10	60 ± 4	133 ± 5	-0.05 ± 0.03	-0.09 ± 0.02
0.17	59 ± 4	122 ± 5	-0.01 ± 0.03	-0.07 ± 0.02
0.30	56 ± 6	112 ± 7	-0.11 ± 0.05	-0.04 ± 0.04
0.50	57 ± 7	85 ± 6	-0.01 ± 0.04	-0.05 ± 0.02
0.80	53 ± 8	96 ± 10	-0.03 ± 0.05	-0.03 ± 0.03
Ground-based (MDM 2.4-m with ModSpec) – Major axis profile				
0.37	15 ± 3	107 ± 6	0.00 ± 0.04	-0.01 ± 0.02
0.74	26 ± 3	93 ± 6	-0.04 ± 0.03	-0.04 ± 0.02
1.30	45 ± 2	92 ± 5	-0.05 ± 0.03	-0.03 ± 0.02
2.04	60 ± 2	94 ± 4	-0.13 ± 0.03	0.05 ± 0.03
3.15	75 ± 3	93 ± 2	-0.14 ± 0.03	0.00 ± 0.03
4.82	83 ± 3	91 ± 4	-0.16 ± 0.05	0.04 ± 0.04
7.42	81 ± 5	104 ± 4	-0.22 ± 0.05	0.10 ± 0.04
11.69	77 ± 7	97 ± 5	-0.19 ± 0.10	0.03 ± 0.06
18.18	70 ± 8	74 ± 7	-0.08 ± 0.06	-0.05 ± 0.03
Ground-based (MDM 2.4-m with ModSpec) – Minor axis profile				
0.00	-4 ± 18	97 ± 6	0.02 ± 0.02	-0.06 ± 0.01
0.37	1 ± 3	103 ± 5	0.01 ± 0.03	-0.06 ± 0.02
0.74	3 ± 2	103 ± 5	-0.02 ± 0.04	-0.07 ± 0.02
1.30	7 ± 2	96 ± 4	-0.02 ± 0.03	-0.03 ± 0.02
2.04	14 ± 2	105 ± 5	0.00 ± 0.04	0.02 ± 0.03
3.15	4 ± 3	109 ± 4	0.11 ± 0.03	-0.05 ± 0.03
4.82	6 ± 3	107 ± 4	0.01 ± 0.04	-0.09 ± 0.03
7.42	14 ± 5	125 ± 6	0.06 ± 0.06	-0.21 ± 0.06
11.69	-6 ± 5	128 ± 6	0.07 ± 0.07	-0.17 ± 0.07
18.18	-58 ± 11	58 ± 14	-0.01 ± 0.05	-0.07 ± 0.03



Table 4. DYNAMICAL MODELS

Model	Mass <sup>a</sup> Profile	Tracer <sup>a</sup> Profile	Kinem. <sup>b</sup> Dataset	$i^c$ ( $^\circ$ )	$\epsilon^d$	$M_\bullet^e$ ( $10^7 M_\odot$ )	$\Upsilon^e$	$\S$
Base	$V_{\text{corr}}$	$V_{\text{corr}}$	S+G	72	0.35	$3.31^{+0.22}_{-0.17}$	$3.6^{+0.1}_{-0.1}$	5.1
D1	$V_{\text{corr}}$	$V_{\text{corr}}$	S+G	72	0.45	$3.48^{+0.42}_{-0.38}$	$3.7^{+0.2}_{-0.2}$	5.2.1
D2	$V_{\text{corr}}$	$V_{\text{corr}}$	S+G	62	0.35	$3.62^{+0.38}_{-0.49}$	$3.8^{+0.1}_{-0.2}$	5.2.2
K1	$V_{\text{corr}}$	$V_{\text{corr}}$	S <sub>1</sub> +G	72	0.35	$3.25^{+0.21}_{-0.13}$	$3.6^{+0.1}_{-0.1}$	5.3
K2	$V_{\text{corr}}$	$V_{\text{corr}}$	S <sub>3</sub> +G	72	0.35	$2.20^{+0.54}_{-0.31}$	$3.6^{+0.1}_{-0.1}$	5.3
K3	$V_{\text{corr}}$	$V_{\text{corr}}$	G	72	0.35	$1.03^{+1.00}_{-0.28}$	$3.7^{+0.1}_{-0.2}$	5.3
K4	$V_{\text{corr}}$	$V_{\text{corr}}$	S+G <sub>1</sub>	72	0.35	$3.33^{+0.21}_{-0.19}$	$3.7^{+0.1}_{-0.1}$	5.3
P1	NIR <sub>corr</sub>	$V_{\text{corr}}$	S+G	72	0.35	$2.49^{+0.09}_{-0.10}$	$3.5^{+0.1}_{-0.1}$	5.4
P2	$V_{\text{corr}}$	NIR <sub>corr</sub>	S+G	72	0.35	$3.33^{+0.18}_{-0.17}$	$3.6^{+0.1}_{-0.1}$	5.4
P3	NIR <sub>corr</sub>	NIR <sub>corr</sub>	S+G	72	0.35	$2.43^{+0.21}_{-0.30}$	$3.5^{+0.1}_{-0.1}$	5.4
P4	$V$	$V$	S+G	72	0.35	$3.25^{+0.22}_{-0.14}$	$3.6^{+0.1}_{-0.1}$	5.4

<sup>a</sup>Mass and tracer profiles named as in Figure 12 (cf. §5.4).

<sup>b</sup>S = All STIS kinematic data listed in Table 3.

S<sub>1</sub> = As in S but without the central kinematic datapoint.

S<sub>3</sub> = As in S but without the 3 central kinematic datapoints.

G = All ground-based (MOSPEC) kinematic data listed in Table 3.

G<sub>1</sub> = As in G but without the central minor-axis datapoint.

<sup>c</sup>Disk inclination (cf. §5.2.2). Edge-on corresponds to  $i = 90^\circ$ .

<sup>d</sup>Isophote ellipticity, assumed constant throughout the galaxy (cf. §5.2.1).

<sup>e</sup>Black hole mass and stellar  $M/L$  ratio ( $\Upsilon$ ), assumed constant throughout the galaxy (cf. §5.1). Uncertainty values correspond to the nominal “ $1\sigma$ ” one-dimensional uncertainties from the contour maps (Figure 14). The  $M/L$  ratio calibration is in the  $V$  band.